Supplementary Materials

Developmentally regulated autophagy is required for eye formation in *Drosophila*

Viktor Billes, Tibor Kovács, Anna Manzéger, Péter Lőrincz, Sára Szincsák, Péter István Kulcsár, Ágnes Regős, Tamás Korcsmáros, Tamás Lukácsovich, Gyula Hoffmann, Miklós Erdélyi, József Mihály, Krisztina Takács-Vellai, Miklós Sass, Tibor Vellai

Supplementary materials include:

Genotypes; Supplementary Tables: S1, S2; Supplementary Figures and Figure Legends: S1 to S31

List of genotypes

Figure 2.

(A to D’’’): w^{1118}

(E to E’’’): *w*; ey-Gal4(II), UAS-mCherry-Atg8a/+*

Figure 3.

(A, A’, A’’’): *w*; ey-Gal4(II)/+*

(A’’): *w*; ey-Gal(II), UAS-mCherry-Atg8a/+*

(B, B’, B’’’): *w*; ey-Gal4(II)/Atg101* RNAi *(KK101226)*

(B’’): *w*; ey-Gal(II), UAS-mCherry-Atg8a/Atg101* RNAi *(KK101226)*

(C, C’, C’’’): *w*; ey-Gal4(II)/Atg14* RNAi

(C’’): *w*; ey-Gal(II), UAS-mCherry-Atg8a/Atg14* RNAi

(D, D’, D’’’): *w*; ey-Gal4(III)/+*

(D’’): *w*; UAS-mCherry-Atg8a/+; ey-Gal4(III)/+*

(E, E’, E’’’): *ey-Gal4(III)/Atg3 RNAi*

(E’’): *w*; ey-Gal4(II), UAS-mCherry-Atg8a/+; Atg3* RNAi/+ (at 18°C)

(F): see Table S1

(G): *ey-Gal4(II)=w*; ey-Gal4(II)/+ Atg101* RNAi=*w*; ey-Gal4(II)/Atg101* RNAi *(KK101226)*. *Atg14* RNAi=*w*; ey-Gal4(II)/Atg14* RNAi. ey-Gal4(III)=*w*; ey-Gal4(III)/+*. *Atg3* RNAi=*w*; ey-Gal4(III)/Atg3* RNAi.

Figure 4.

(A’ to D): w^{1118} and $Atg8a^{KG07569}$.

(E): w^{1118} and $Atg18a^{KG03090}$*/Atg18a Df(3L)Exel6112*. (*Atg18a* Df(3L)Exel6112 is a large deletion overlapping the genomic region of *Atg18a*)

(F): w^{1118} and $Atg4^{MB03551}$

(G to G’’’’): RNAi control = w*; *ey-Gal4(II), UAS-Dcr-2/+*. *Atg8a* RNAi = w*; *ey-Gal4(II), UAS-Dcr-2/+; Atg8a* RNAi/+

(H, H’): Non-green cells: *w*, ey-FLP; FRT82B, $Atg17^{d130}$*. Green cells: *w*, ey-FLP; FRT82B, Ubi-GFP* or *w*, ey-FLP; FRT82B, $Atg17^{d130}$/FRT82B, Ubi-GFP*

(I, I’): non-green cells: *w*, ey-FLP; $Atg1^{KG07993}$, FRT80B*. Green cells: *w*, ey-FLP; Ubi-GFP, FRT80B* or *w*, ey-FLP; Ubi-GFP, FRT80B / $Atg1^{KG07993}$, FRT80B.*

Figure 5. *$Atg14^{\Delta 5.2}$ = ey-Gal4, UAS-FLP/+; FRT82B, Atg14Δ5.2/FRT82B, GMR-hid, l(3)CL-R1*

Atg14 RNAi = *Atg14* RNAi*/ey-Gal4, UAS-FLP; FRT82B/FRT82B, GMR-hid, l(3)CL-R1*

Atg14 RNAi*; $Atg14^{\Delta 5.2}$ = Atg14* RNAi*/ey-Gal4, UAS-FLP; FRT82B, Atg14Δ5.2/FRT82B, GMR-hid, l(3)CL-R1*

Figure 6.

ey-Gal4(II) = *w*; ey-Gal4(II)/+*. *Atg101* RNAi = *w*; ey-Gal4(II)/Atg101* RNAi *(KK101226)*. *Atg14* RNAi = *w*; ey-Gal4(II)/Atg14* RNAi. ey-Gal4(III) = *w*; ey-Gal4(III)/+*. *Atg3* RNAi = *w*; ey-Gal4(III)/Atg3* RNAi.

Figure 7.

(C, D, F): *w^{1118}*

(F'): *w^{1118}; eGFP-Atg8a-A (attP-58A)*

(G): *w^{1118}; eGFP-Atg8a-A (attP-51C)*

(G'): *w^{1118}; $_{mutlab}$eGFP-Atg8a-A (attP-51C)*

(G''): *w^{1118}; $_{mutHox}$eGFP-Atg8a-A (attP-51C)*

(H to H''''): *eGFP-Atg8a-A* = w*; *eGFP-Atg8a-A (attP-58A)/ey-Gal4(II), UAS-Dcr-2*. *eGFP-Atg8a-A, lab* RNAi = w*; *lab* RNAi, *eGFP-Atg8a-A (attP-58A)/ ey-Gal4(II), UAS-Dcr-2*. *$_{mutlab}$eGFP-Atg8a-A* = w*; *$_{mutlab}$eGFP-Atg8a-A (attP-58A)/ey-Gal4(II), UAS-Dcr-2*. *$_{mutlab}$eGFP-Atg8a-A, lab* RNAi = w*; *lab* RNAi, *$_{mutlab}$eGFP-Atg8a-A (attP-58A)/ey-Gal4(II), UAS-Dcr-2*

(I to I''''): eGFP-Atg8a-A = *w*; eGFP-Atg8a-A (attP-51C)/+; ey-Gal4(III)/+*. *eGFP-Atg8a-A; UAS-lab = w*; eGFP-Atg8a-A (attP-51C)/UAS-lab; ey-Gal4(III)/+*. *$_{mutlab}$eGFP-Atg8a-A = w*; $_{mutlab}$eGFP-Atg8a-A (attP-51C)/+; ey-Gal4(III)/+*. *$_{mutlab}$eGFP-Atg8a-A; UAS-lab = w*; $_{mutlab}$eGFP-Atg8a-A (attP-51C)/UAS-lab; ey-Gal4(III)/+*.(J) *w*; ey-Gal4(II), UAS-Dcr-2/+*, (J''-J'''): lab RNAi = *w*; lab* RNAi*/ey-Gal4(II), UAS-Dcr-2*

(J): *w*; ey-Gal4(II), UAS-Dcr-2/+*.

Figure 8.

(A): *w*; ey-Gal4(III)/+* and *w*; lab* RNAi*/+; ey-Gal4(III)/UAS-Dcr-2*

(B): UAS-lab = *w*; UAS-lab/+; ey-Gal4(III)/+*. *lab* RNAi = *w*; lab* RNAi*/+; ey-Gal4(III)/UAS-Dcr-2*.

Figure 9.

(A, A', A''' to A'''''): *w*; ey-Gal4(III)/+*

(A''): *w*; UAS-mCherry-Atg8a/+; ey-Gal4(III)/+*

(B, B', B''' to B''''' and H): *w*; UAS-lab/+; ey-Gal4(III)/+*

(B''): *w*; UAS-mCherry-Atg8a/UAS-lab; ey-Gal4(III)/+*

(C, C', C''' to C'''''): *w*; ey-Gal4(II), UAS-Dcr-2/+*

(A'''): *w*; UAS-mCherry-Atg8a/ey-Gal4(II), UAS-Dcr-2*

(D, D', D''' to D'''''): *w*; ey-Gal4(II), UAS-Dcr-2/lab* RNAi

(A'''): *w*; ey-Gal4(II), UAS-mCherry-Atg8a/lab* RNAi*; UAS-Dcr-2/+*

(E to G): *ey-Gal4(III)* = w*; *ey-Gal4(III)/+*. *UAS-lab* = w*; *UAS-lab/+; ey-Gal4(III)/+*. *ey-Gal4(II)* = w*; *UAS-Dcr-2; ey-Gal4(II)/+*. *lab* RNAi = w*; *ey-Gal4(II), UAS-Dcr-2/lab* RNAi; FRT82B = w*, *ey-FLP*; *FRT82B, l(3)cl-$R3^1$/FRT82B. lab^4 = ey-FLP; FRT82B, l(3)cl-$R3^1$/FRT82B, lab^4*. *l(3)cl-$R3^1$* is a lethal mutation causing the loss of homozygous cells. This latter system leads to eye discs nearly homozygous for *lab^4*.

Supplementary Tables

Tables S1. Depletion of Atg proteins in the eye disc can severely compromise the development of the organ.

Gene	*Gal4* driver, UAS construct	Ratio of eye phenotypes (%)	Total amount of samples	Eye phenotype				Sex	T
				Wild-type	Aberrant	Small	Eyeless		
-	*ey-Gal4(II)/+*	0	332	332	0	0	0	F	29°C
		0	286	286	0	0	0	M	29°C
-	*ey-Gal4(II)*	0	362	362	0	0	0	F	25°C
		0	304	304	0	0	0	M	25°C
Dcr-2 overexpr.	*ey-Gal4(II); UAS-Dcr-2/+*	0	386	386	0	0	0	F	29°C
		0	284	284	0	0	0	M	29°C
***eGFP* #1**	*ey-Gal4(II)/+; $eGFP^{pVALIUM20shRNA}$(III)/+*	0	348	348	0	0	0	F	29°C
		0	240	240	0	0	0	M	29°C
***eGFP* #2**	*ey-Gal4(II)/+; $eGFP^{pVALIUM22shRNA}$(III)/+*	0	118	118	0	0	0	F	29°C
		0	88	88	0	0	0	M	29°C
***eGFP* #3**	*ey-Gal4(II)/$eGFP^{pVALIUM22shRNA}$(II)*	0	136	136	0	0	0	F	29°C
		0	2	2	0	0	0	M	29°C
Atg1	*ey-Gal4(II); $Atg1^{JF02273}$*	0.00	136	136	0	0	0	F	25°C
		8.73	126	115	7	4	0	M	25°C
Atg2	*ey-Gal4(III)/$Atg2^{HMS01198}$*	20.45	132	105	4	23	0	F	29°C
		100	36	0	1	33	2	M	29°C
	ey-Gal4(II); UAS-Dcr-2/UAS-Dcr-2; $Atg2^{JF02786}$/+	10	70	63	0	7	0	F	29°C
		33.33	36	24	0	12	0	M	29°C
Atg3	*ey-Gal4(III)/$Atg3^{HMS01348}$*	82.43	74	13	14	41	6	F	29°C
		93.1	58	4	3	51	0	M	29°C
Atg4a	*ey-Gal4(II); $Atg4a^{JF03003}$*	0	244	244	0	0	0	F	25°C
		3.9	308	296	5	6	1	M	25°C
Atg5	*ey-Gal4(II); $Atg5^{JF02703}$*	0	80	80	0	0	0	F	25°C
		13.39	112	97	4	10	1	M	25°C
Atg6	*ey-Gal4(II); UAS-Dcr-2/UAS-Dcr-2; $Atg6^{JF02897}$/+*	100	102	0	0	102	0	F	29°C
		100	64	0	0	64	0	M	29°C
Atg7	*ey-Gal4(II); $Atg7^{JF02787}$*	0	322	322	0	0	0	F	25°C
		1.61	496	488	1	7	0	M	25°C
Atg8a	*ey-Gal4(II); UAS-Dcr-2/+; $Atg8a^{GD4654}$/+*	17.75	845	695	26	123	1	F	29°C
		50.6	500	247	32	216	5	M	29°C
	ey-Gal4(II); UAS-Dcr-2/+; $Atg8a^{JF02895}$/+	15.22	473	401	31	41	0	F	29°C
		42.99	328	187	22	119	0	M	29°C
Atg8b	*ey-Gal4(II)/+; $Atg8b^{HMS01245}$/+*	0	222	222	0	0	0	F	29°C
		6.08	148	139	0	9	0	M	29°C
Atg9	*ey-Gal4(II); $Atg9^{JF02891}$*	0	508	508	0	0	0	F	25°C
		2.88	800	777	6	17	0	M	25°C
Atg10	*ey-Gal4(II)/$Atg10^{HMS02026}$*	0	128	128	0	0	0	F	29°C
		0	84	84	0	0	0	M	29°C
Atg12	*$Atg12^{KK111564}$; ey-Gal4(III)*	0	226	226	0	0	0	F	29°C
		1.09	92	91	0	1	0	M	29°C

Atg13	*ey-Gal4(II); Atg13^{KK100340}*	0	268	268	0	0	0	F	25°C
		0.31	320	319	0	1	0	M	25°C
Atg14	*ey-Gal4(II); UAS-Dcr-2/Atg14^{KK100903}*	78.26	46	10	0	25	11	F	25°C
		pupal lethal						M	25°C
Atg16	*ey-Gal4(II)/+; Atg16^{HMS01347}/+*	0.68	146	145	0	1	0	F	29°C
		1.67	120	118	0	2	0	M	29°C
Atg17	*Atg17^{KK101847}; ey-Gal4(III)*	0.42	238	237	0	1	0	F	29°C
		0	222	222	0	0	0	M	29°C
Atg18a	*ey-Gal4(II); Atg18a^{JF02898}*	0	70	70	0	0	0	F	25°C
		1.59	126	124	2	0	0	M	25°C
Atg101	*ey-Gal(II); UAS-Dcr-2/Atg101^{KK101226}*	96.67	60	2	0	49	9	F	29°C
		100	6	0	0	5	1	M	29°C
Vps15	*ey-Gal4(II)/+; Vps15^{HMS00908}/+*	45.65	46	25	0	21	0	F	29°C
		83.33	6	1	0	5	0	M	29°C
Pi3K59F /Vps34	*ey-Gal4(II)/+; Vps34^{GL00175}/+*	0	244	244	0	0	0	F	29°C
		0.44	226	225	1	0	0	M	29°C

RNAi constructs that work effectively (*i.e.* decrease transcript levels) cause severe, highly penetrant defects in eye development. Those affecting eye development with a relatively high percentage (over 50%) are highlighted by yellow coloring. overexpr., overexpression; F, female; M, male; T, temperature.

Table S2. Depletion of Atg proteins only in the peripodial membrane does not affect eye development.

Gene	**UAS construct**	**Ratio of aberrant eyes (%)**	**Total amount of eyes observed**	**Eye phenotype**			**Sex**	**T**
				Wild-type	**Small**	**Eyeless**		
eGFP #1	*eGFP$^{pVALIUM20shRNA(III)}$*	1.84	326	320	5	1	F	29°C
		1	200	198	2	0	M	29°C
eGFP #3	*eGFP$^{pVALIUM22shRNA(II)}$*	0.77	392	389	3	0	F	29°C
		0	76	76	0	0	M	29°C
Atg1	*Atg1^{HMS02750}*	0.36	558	556	1	1	F	29°C
		0	494	494	0	0	M	29°C
Atg2	*Atg2^{HMS01198}*	larval lethal					F	29°C
		larval lethal					M	29°C
Atg3	*Atg3^{HMS01348}*	larval lethal					F	29°C
		larval lethal					M	29°C
Atg4a	*Atg4a^{HMS01482}*	0.88	114	113	1	0	F	29°C
		0	68	68	0	0	M	29°C
Atg5	*Atg5^{HMS01244}*	0	102	102	0	0	F	29°C

		0	90	90	0	0	M	29°C
Atg6	*Atg6*^{HMS01483}	0	156	156	0	0	F	29°C
		0	92	92	0	0	M	29°C
Atg7	*Atg7*^{HMS01358}	1	100	99	1	0	F	29°C
		0	94	94	0	0	M	29°C
Atg8a	*Atg8a*^{HMS01328}	0.31	324	323	1	0	F	29°C
		0.43	234	233	1	0	M	29°C
Atg8b	*Atg8b*^{HMS01245}	0	298	298	0	0	F	29°C
		0	174	174	0	0	M	29°C
Atg9	*Atg9*^{HMS01246}	1.64	366	360	5	1	F	29°C
		0.91	110	109	1	0	M	29°C
Atg10	*Atg10*^{HMS02026}	0	162	162	0	0	F	29°C
		0	132	132	0	0	M	29°C
Atg12	*Atg12*^{HMS01153}	1.12	178	176	2	0	F	29°C
		0.88	114	113	1	0	M	29°C
Atg13	*Atg13*^{HMS02028}	0	432	432	0	0	F	29°C
		0	410	410	0	0	M	29°C
Atg14	*Atg14*^{KK100903}	0.39	254	253	1	0	F	29°C
		0	44	44	0	0	M	29°C
Atg16	*Atg16*^{HMS01347}	0	156	156	0	0	F	29°C
		0	158	158	0	0	M	29°C
Atg18a	*Atg18a*^{HMS01193}	0.98	410	406	2	2	F	29°C
		0	264	264	0	0	M	29°C
Atg101	*Atg101*^{KK101226}	0	120	120	0	0	F	29°C
		0	12	12	0	0	M	29°C
	Atg101^{HMS01349}	0	28	28	0	0	F	29°C
		pupal lethal					M	29°C
		0	60	60	0	0	F	25°C
		0	54	54	0	0	M	25°C
Vps15	*Vps15*^{HMS00908}	pupal lethal					F	29°C
		pupal lethal					M	29°C
		0	60	60	0	0	F	25°C
		0	76	76	0	0	M	25°C
	Vps15^{GL00085}	0.36	560	558	1	1	F	29°C
		0	78	78	0	0	M	29°C
Pi3K59F/ Vps34	*Pi3K59F/Vps34*^{HMS00261}	0	222	222	0	0	F	29°C
		0	10	10	0	0	M	29°C

F, female; M, male; T, temperature.

Supplementary Figures

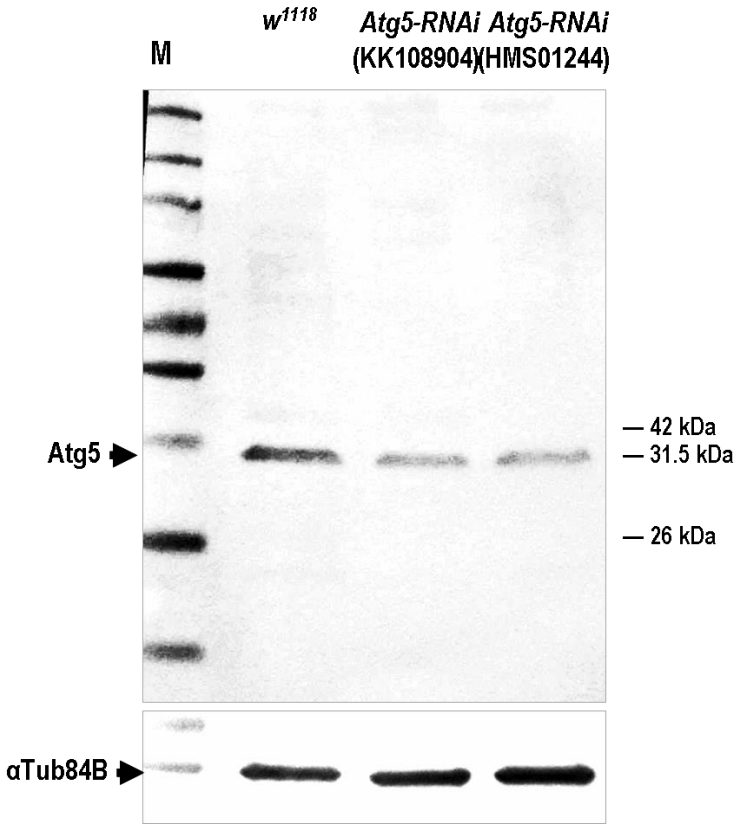

Figure S1. Western blot analysis showing the specificity of the Atg5 antibody used in this study. A single Atg5-specific band is visible (upper arrow) that is weaker in *Atg5* RNAi backgrounds. w^{1118}, control sample. Protein samples were isolated from fat bodies of well-fed L3 staged larvae (76 to 90 h). αTub84B (α-Tubulin at 84B) was used as an internal control. M, molecular mass marker.

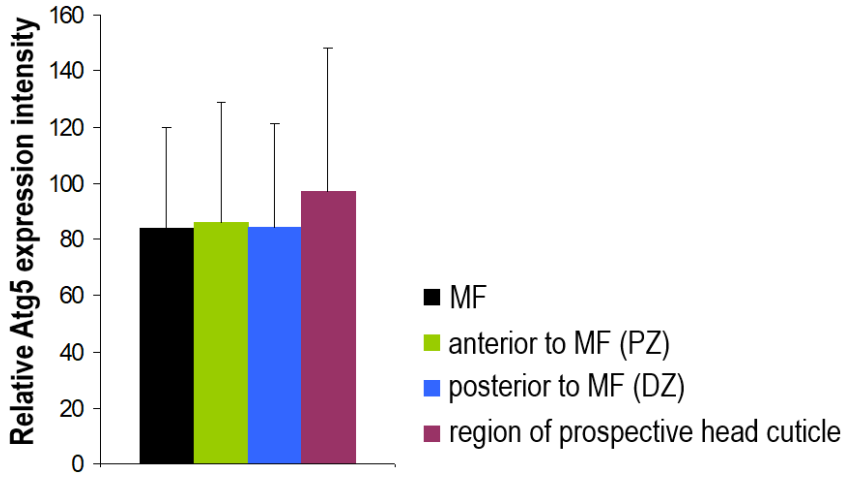

Figure S2. Ubiquitous accumulation of Atg5 in the eye disc. Relative Atg5 protein levels were determined in different regions of the eye disc. Bars represent mean ±S.D., no significant change was detected among the regions examined. MF, morphogenetic furrow; PZ, proliferation zone; DZ, differentiation zone. Genotype: w^{1118}.

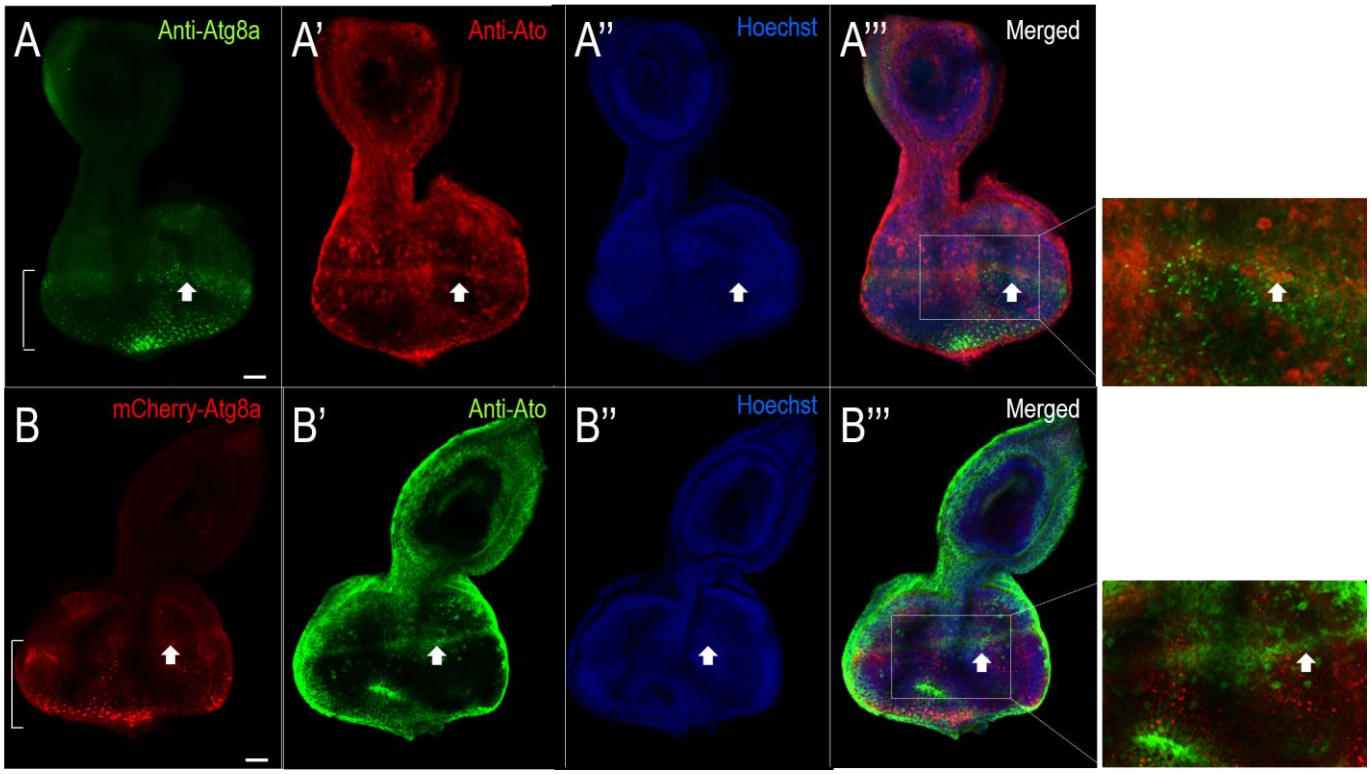

Figure S3. Accumulation of Atg8a-positive autophagic structures in the eye disc. (**A**) Anti-Atg8a antibody staining shows green foci labeling autophagic structures predominantly in the MF and DZ. (**A'**) Anti-Atonal (Ato) antibody staining (red) show the area of MF. (**A''**) Hoechst staining (blue) indicates nuclei. (**A'''**) Merged image. (**B**) Autophagic structures (red foci) labeled by an mCherry-Atg8a reporter. (**B'**) Atonal-specific antibody staining (green) indicates the MF. (**B''**) Hoechst staining (blue) shows nuclei. (**B'''**) Merged image. Pictures in panels **A** to **B'''** were made by confocal microscopy; bars: 10 µm. The bracket indicates the regions of the morphogenetic furrow (MF) and differentiation zone (DZ), the arrow points to the MF. Genotype in (**A** to **A'''**): w^{1118}; (**B** to **B'''**): *w*; ey-Gal4(II)/UAS-mCherry-Atg8a.*

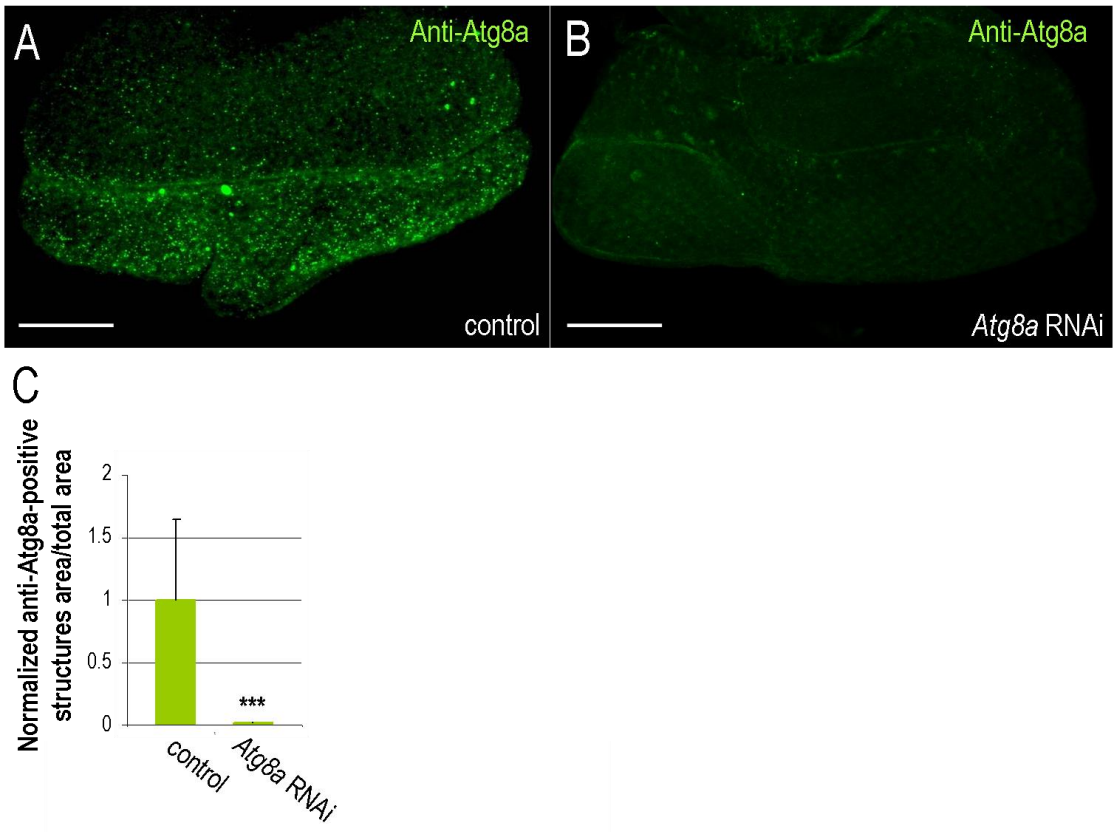

Figure S4. The Anti-Atg8a antibody used in this study specifically labels autophagic structures. (**A**) Anti-Atg8a antibody staining on a control eye disc labels autophagic structures (green foci). (**B**) Anti-Atg8a antibody staining fails to detect autophagic structures in an *Atg8a* RNAi eye disc. (**C**) Quantification of Atg8a-positive structures in control (untreated) versus *Atg8a* RNAi eye disc samples. Bars represent mean ±S.D., ***: $P<0.001$, Mann-Whitney U-test. In panels **A** to **B**, antenna part is up; bars: 50 µm. Samples were dissected from L3W larvae. control = *w*; ey-Gal4(II), UAS-Dcr-2/+*. *Atg8a* RNAi = *w*; ey-Gal4(II), UAS-Dcr-2/+; Atg8a* RNAi (*GD4654) /+*.

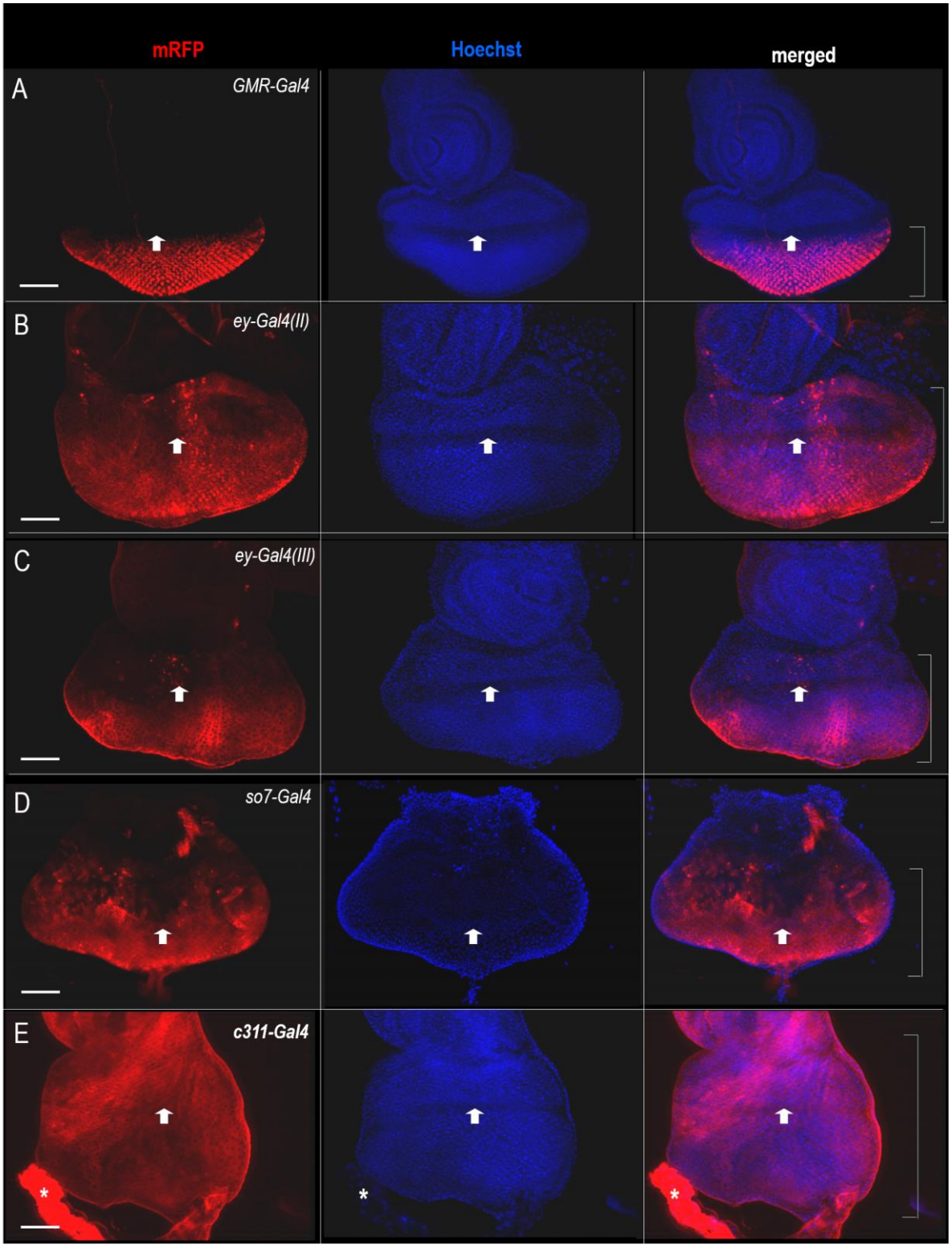

Figure S5. Expression domain of eye-specific *Gal4* drivers used in this study. (**A**) Expression of *GMR-Gal4* in the eye disc is restricted to the differentiation zone. No expression is

detectable in the morphogenetic furrow (MF) and proliferation zone, *i.e.* in front of the MF. (**B**) The broad expression domain of *ey-Gal4(II)* in the eye disc includes each major part of the organ. (**C**) Expression of *ey-Gal4(III)* in the eye disc is evident only in the MF and differentiation zone (behind the MF). A few cell rows in front of the MF also express the reporter. (**D**) Expression of *so7-Gal4* in the eye disc. Reporter activity is evident in almost the entire organ. (**E**) Expression of *c311-Gal4* is detectable only in the peripodial membrane. This driver is highly expressed in the optic stalk (signed by asterisk). In each panel, the white arrow indicates the MF, Hoechst staining (blue) shows nuclei, brackets in the merged pictures designate the extent of expression domains, antenna part is up; bars: 50 µm. *UAS-Apoliner* was used as the source of mRFP. Heterozygous animals were examined.

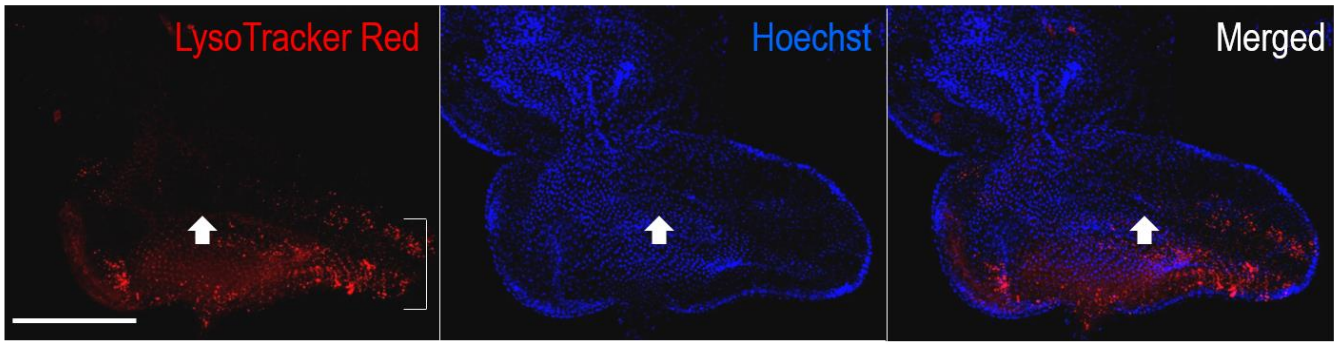

Figure S6. LysoTracker Red staining indicates acidic compartments in the eye disc. Images are positioned as the antenna part is up, the bar represents 100 µm, and the arrow indicates the position of the morphogenetic furrow. The sample was prepared from an L3W larva. Hoechst staining (blue) indicates nuclei. Acidic compartments (autophagosomes, autolysosomes and multivesicular bodies) predominantly accumulate in the MF and differentiation zone (bracket). Genotype: w^{1118}.

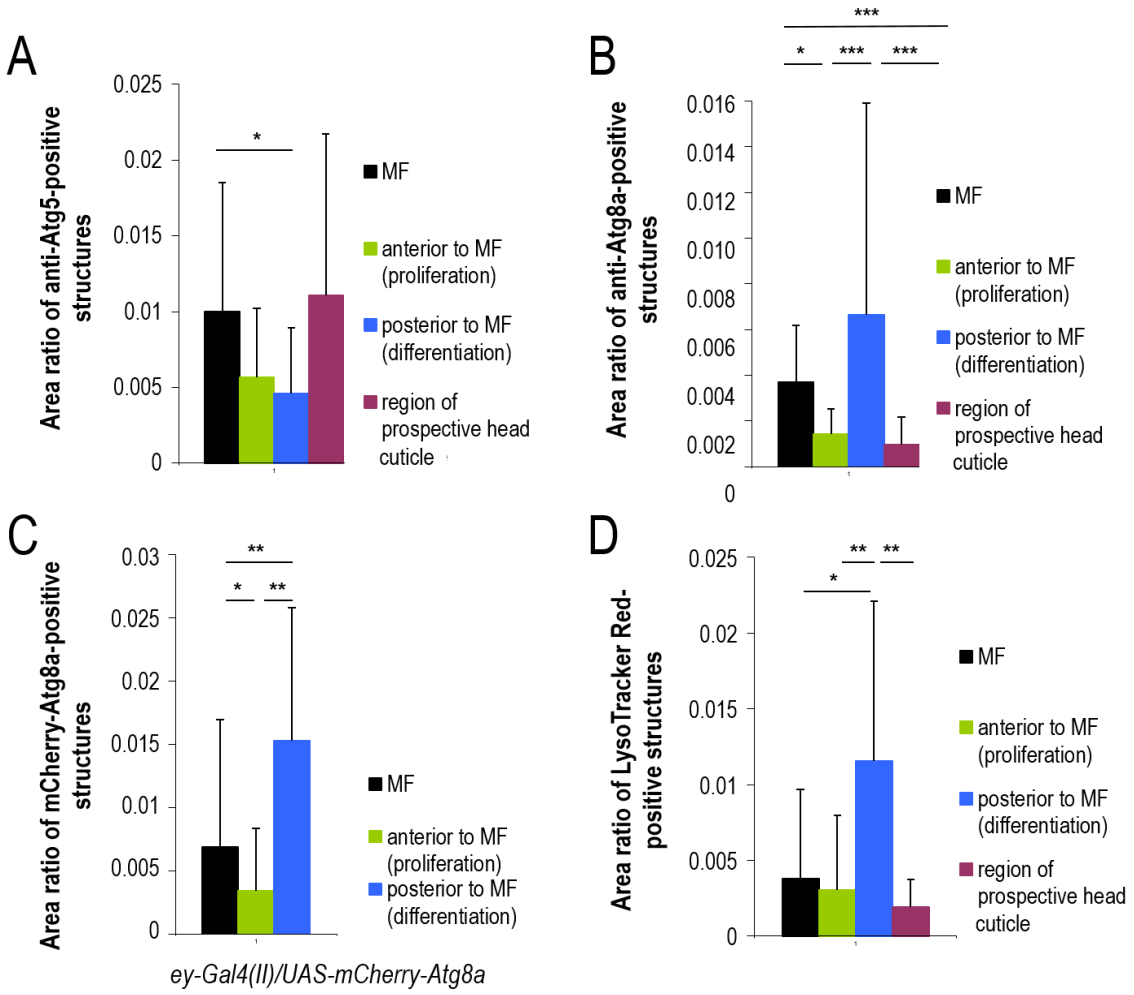

Figure S7. Relative amount of autophagic structures in different regions of the eye disc. (**A**) The amount of Atg5-specific foci in different parts of the eye disc. (**B**, **C**) Relative amount of Atg8a-specific structures in the main parts of the eye disc. Anti-Atg8a staining (**B**) and *mCherry-Atg8a* reporter expression (**C**) are specific to autophagic compartments. (**D**) Relative amount of LysoTracker Red-positive acidic structures in different parts of the eye disc. Samples were prepared from L3W larvae. According to the combined data, autophagic structures predominantly accumulate within the morphogenetic furrow (MF) and differentiation zone (DZ) (posterior to MF). Bars represent mean ±S.D.; *: $P<0.05$, **:

P<0.01, ***: *P*<0.001, two-sample Student *t* test, *t* test for unequal variances or Mann-Whitney U test. Genotype in (A, B, D): w^{1118} (C): *w*; ey-Gal4(II)/ UAS-mCherry-Atg8a*. The number of samples ranged between 4 and 16.

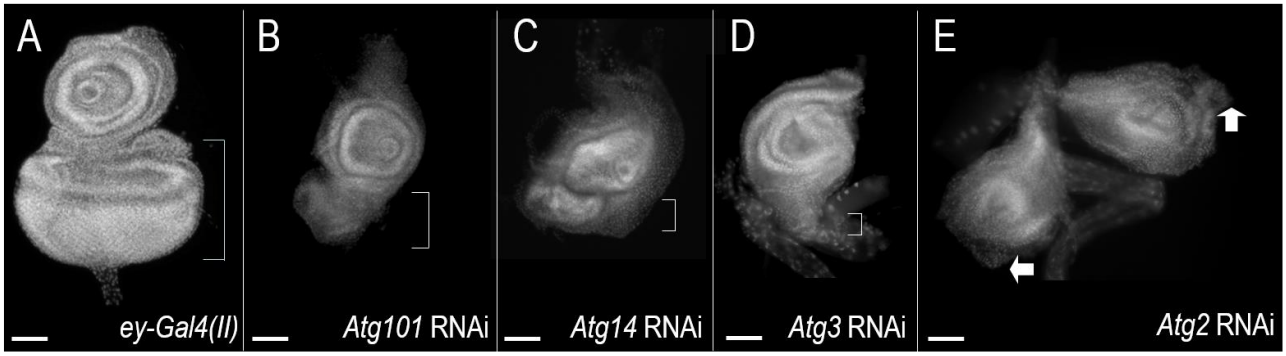

Figure S8. Silencing of *Atg* genes in the eye disc can severely compromise the shape and size of the organ. (**A**) Eye disc sample expressing *ey-Gal4(II)* only (control) shows normal morphology. (**B** to **E**) Morphological defects in *Atg* RNAi eye disc samples. Brackets indicate the area of the eye field. In panel **E**, white arrows show where the eye field should be located. Samples were prepared from L3W larvae, antenna part is up; bars: 50 µm. Genotypes: **A**, *w*; ey-Gal4(II)/+*; **B**, *w*; ey-Gal4(II), UAS-Dcr-2/Atg101* RNAi *(KK101226)*; **C**, *w*; ey-Gal4(II), UAS-Dcr-2/Atg14* RNAi; **D**, *w*; ey-Gal4(II)/+; Atg3* RNAi/+; **E**, *w*; ey-Gal4(II)/+; Atg2* RNAi *(HMS01198)/+*.

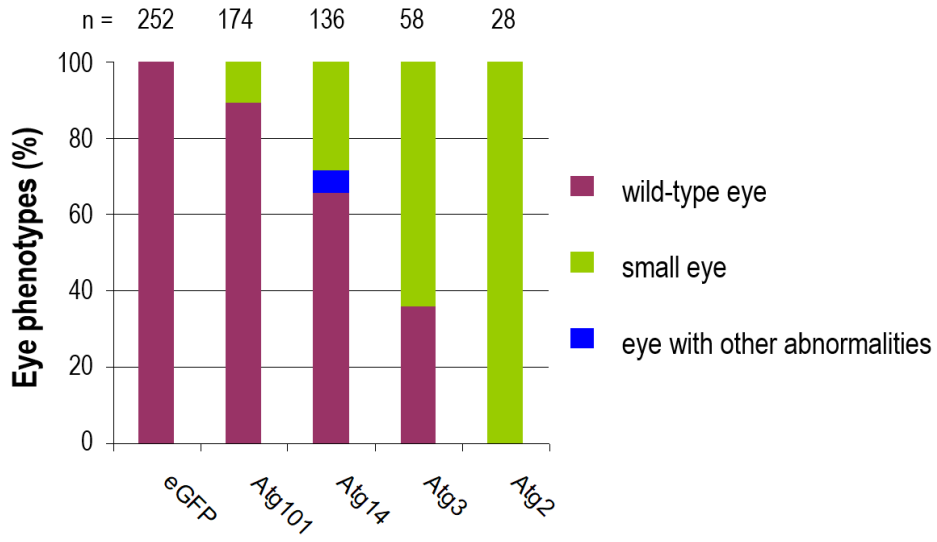

Figure S9. Silencing of *Atg* genes by the *so7-Gal4* driver can cause severe defects in eye development. *so7-Gal4* is active in almost the entire eye disc (also see **Fig. S5D**). eGFP = *eGFP*^{pVALIUM20shRNA}*(III)/so7-Gal4.* Atg101 = *Atg101* RNAi *(KK101226)/+; so7-Gal4/+*. Atg14 = *Atg14* RNAi */+; so7-Gal4/+* Atg3 = *Atg3* RNAi*/so7-Gal4*. Atg2 = *Atg2* RNAi *(HMS01198)/so7-Gal4*.

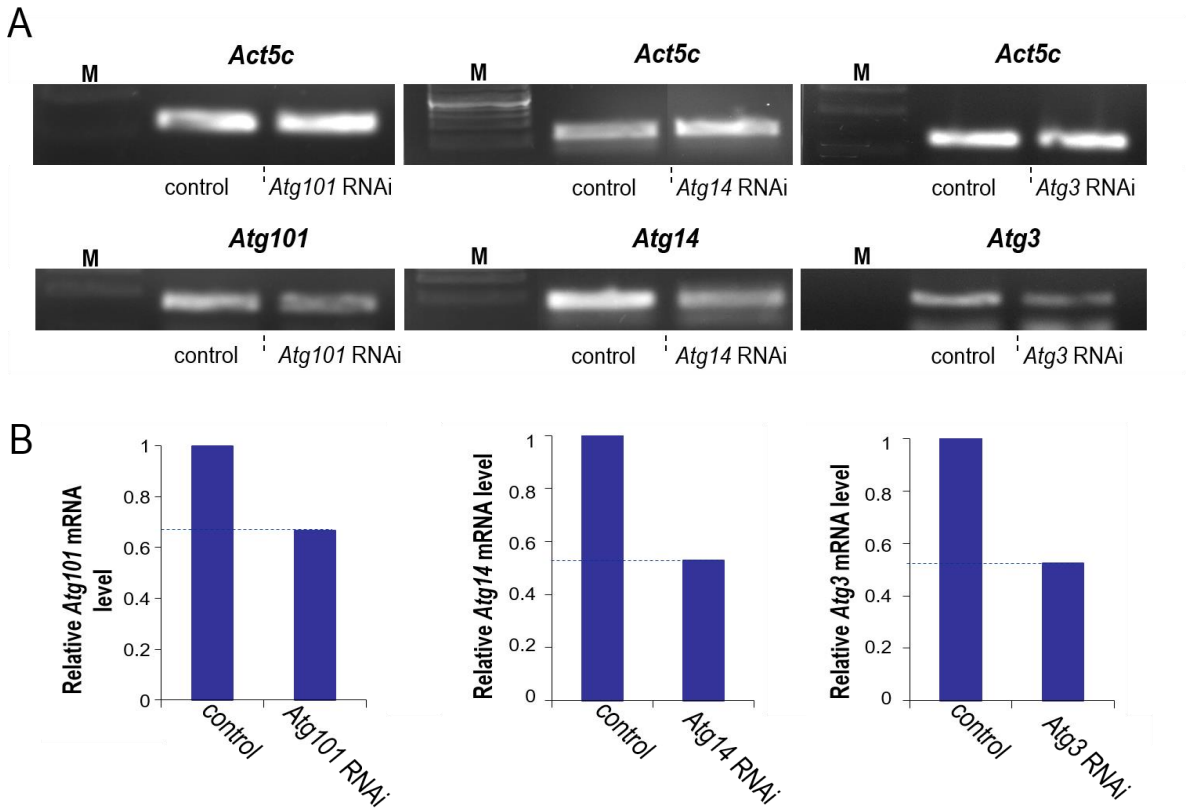

Figure S10. Effective *Atg* RNAi constructs causing defects in eye development significantly reduce the level of the corresponding *Atg* transcripts in the eye disc. (**A**) Semi-quantitative RT-PCR analysis showing that *Atg101*-, *Atg14*- and *Atg3*-specific RNAi constructs markedly (nearly by half) lower the amount of transcripts in the eye disc (bottom images). *Act5C/Actin5c* was used as an internal control (upper images). M, molecular weight marker. (**B**) Quantification of band intensities shown in panel **A**. Control for *Atg101* RNAi and *Atg14* RNAi = *w*; ey-Gal4(II)/+*. *Atg101* RNAi = *w*; ey-Gal4(II)/Atg101* RNAi *(KK101226). Atg14* RNAi = *w*; ey-Gal4(II)/Atg14* RNAi. control for *Atg3* RNAi = *w*; ey-Gal4(III)/+*. *Atg3* RNAi = *w*; ey-Gal4(III)/Atg3* RNAi.

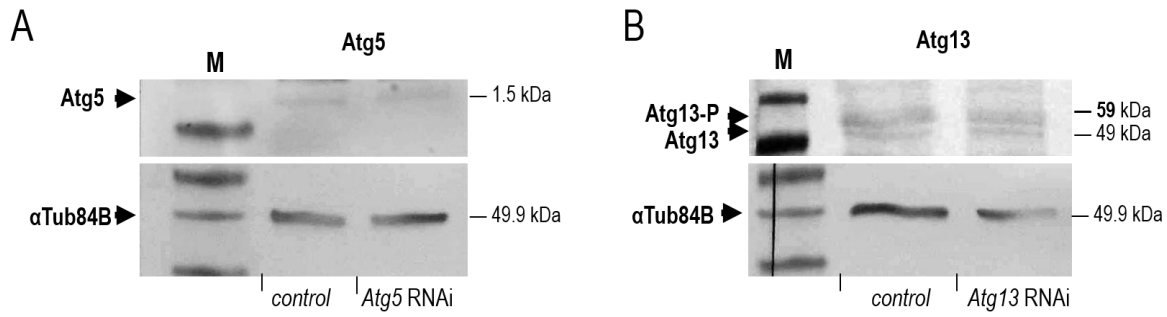

Figure S11. Ineffective *Atg* RNAi constructs causing no defect in eye development do not, or very weakly, alter the amount of the corresponding Atg proteins in the eye disc. Western blot analysis showing the relative amount of Atg5 (**A**) as well as Atg13 and Atg13-P (**B**) proteins, as compared with control samples. Eye-antennal discs were dissected from L3W larvae. αTub84B was used as an internal control. M, molecular mass marker. Genotypes: Control = *w*; ey-Gal4(II), UAS-Dcr-2/+*. *Atg5* RNAi = *w*; ey-Gal4(II), UAS-Dcr-2/+; Atg5* RNAi *(JF02703)/+*. *Atg13* RNAi = *w*; ey-Gal4(II), UAS-Dcr-2/Atg13* RNAi.

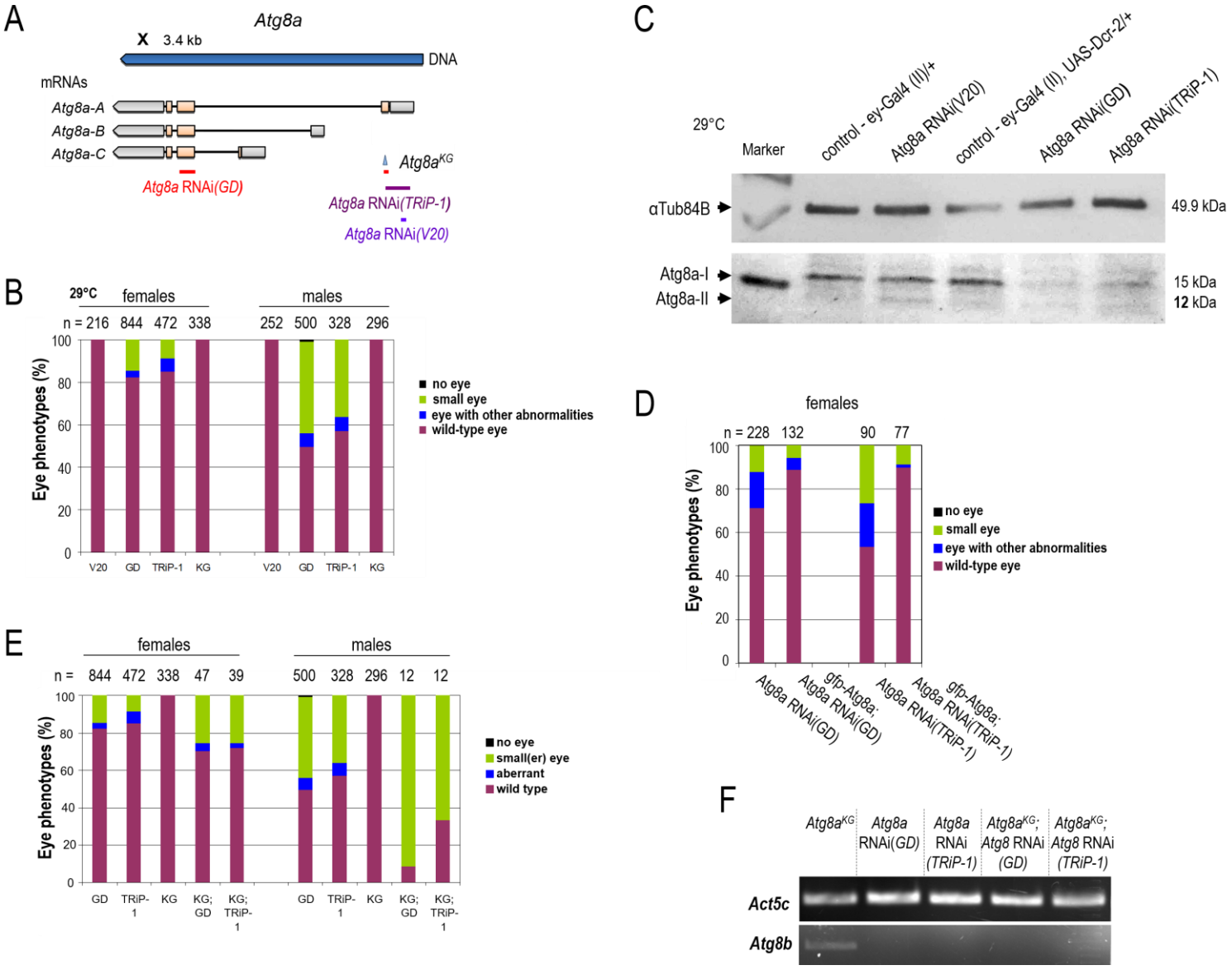

Figure S12. Silencing of *Atg8a* can lead to defects in eye development. (**A**) The transcript isoforms of *Atg8a* (*A*, *B* and *C*) and genomic sites that were targeted by RNAi constructs and the mutation *KG* (*Atg8a*^{KG03090}) are indicated. (**B**) The penetrance of eye phenotypes caused by RNAi treatment and the *KG* mutation. The RNAi construct *V20* and mutation *KG* are proved to be ineffective. (**C**) Levels of Atg8a isoforms (soluble I and PE-conjugated II) in control and RNAi-treated eye samples. (Ineffective) *V20* is not capable of reducing protein levels, whereas (effective) *GD* and *TRiP-1* markedly lowered their accumulation. (**D**) The eye

phenotypes of *Atg8a* RNAi*(GD)* and -*(TRiP-1)* animals can be partially rescued by a transgene containing a full copy of wild-type *Atg8a*. (**E**) Silencing of *Atg8a* by the RNAi construct *GD* and *TRiP-1* in the $Atg8a^{KG}$ mutant background causes a synergistic effect: *RNAi-KG* "double" inhibited animals display defects in eye development with a higher penetrance than the RNAi treatments alone. This may result from the activity of various splice variants (*A*, *B* and *C*) and/or paralogs (*Atg8a* and *Atg8b*). (**F**) Semi-qPCR analysis shows that *Atg8a* RNAi*(GD)* and *Atg8a* RNAi*(TRiP-1)* constructs also eliminate *Atg8b* transcripts. Note that *Atg8b* mRNA is absent in wild-type eye disc (**Fig. 4B**) but is upregulated in $Atg8a^{KG}$ mutant background. In the latter, *GD* and *TRiP-1* RNAi constructs trigger its degradation. *Act5C* was used as an internal control.

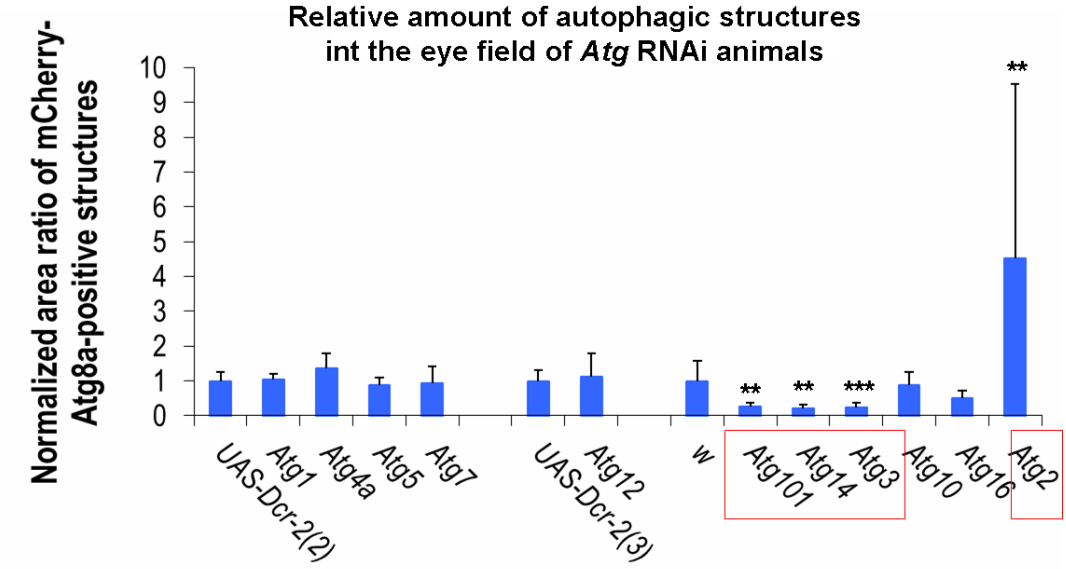

Figure S13. *Atg* RNAi constructs that do not alter eye development are incapable of reducing the relative amount of autophagic structures in this organ. Red frames indicate samples with significant changes. These *Atg* RNAi constructs lead to an obvious eye phenotype. The other constructs proved ineffective to reduce the amount of autophagic structures and to influence eye development. *w*, w^{1118} (control). Bars represent mean ±S.D., **: $P<0.01$, ***: $P<0.001$, two-sample Student t test, t test for unequal variances or Mann-Whitney U test. *Atg1*, *Atg4a*, *Atg5* and *Atg7* RNAi constructs were coexpressed with *UAS-Dcr-2(II)*. Expression of *UAS-Dcr-2(II)* alone served as a control. *Atg12* RNAi was coexpressed with *UAS-Dcr-2(III)*. Expression of *UAS-Dcr-2(III)* alone served as a control. For $Atg101^{KK101226}$-, *Atg14*, *Atg3*, *Atg10*, *Atg16*, and *Atg2* RNAi constructs, *w* (w^{1118}) served as control. In each cross, male genotype was *w*; ey-Gal4(II), UAS-mCherry-Atg8a*.

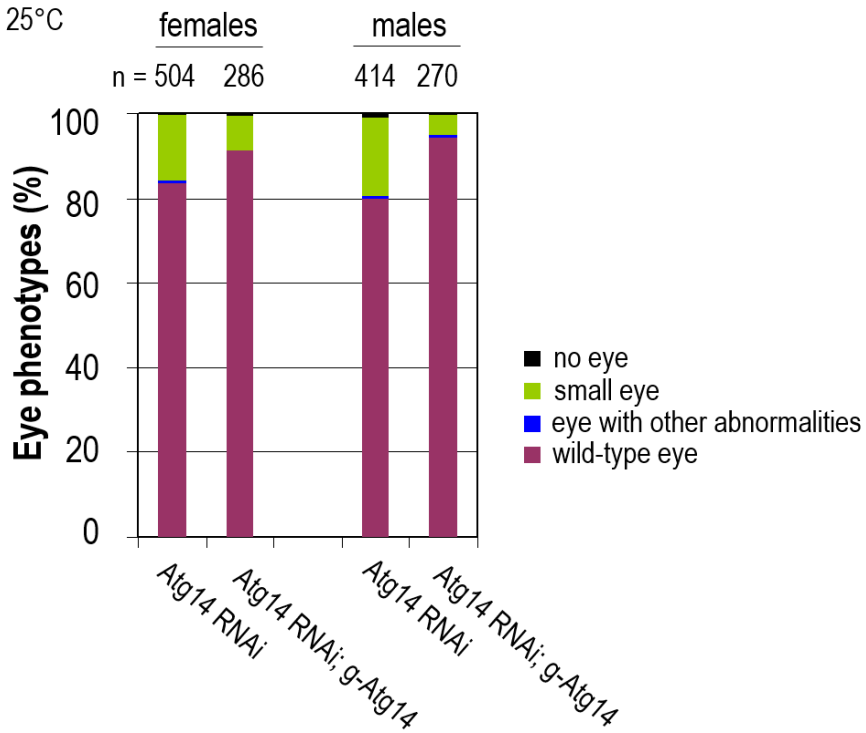

Figure S14. Normal eye development can be rescued in *Atg14* RNAi animals by a transgene containing the wild-type copy of *Atg14*. *g-Atg14* transgene contains a wild-type copy of *Atg14*. It can suppress the mutant eye phenotype by nearly half in *Atg14* RNAi animals. Genotypes: *Atg14* RNAi = *w*; ey-Gal4(II)/Atg14* RNAi. *Atg14* RNAi, *g-Atg14* = *w*; ey-Gal4(II)/Atg14* RNAi*; g-Atg14/+*.

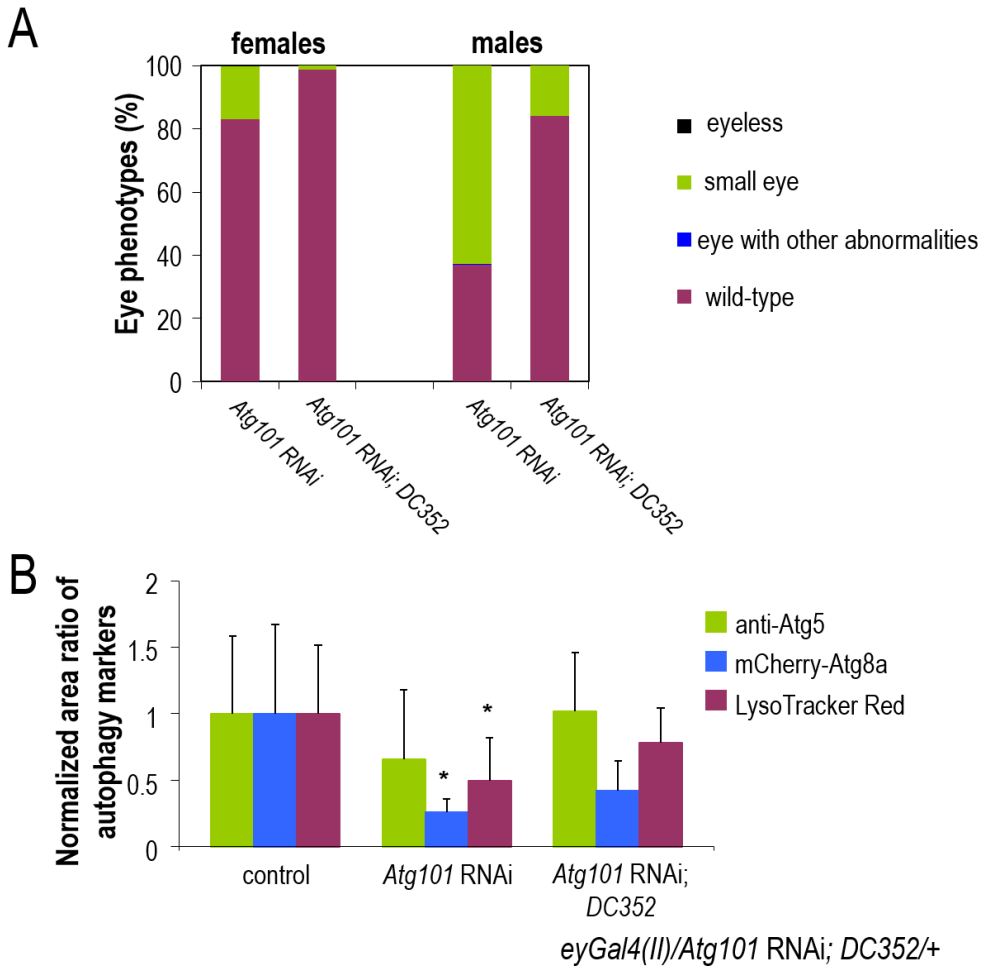

Figure S15. A duplication covering the *Atg101* locus can rescue normal eye development in *Atg101* RNAi animals. (**A**) Penetrance of the eye phenotype in *Atg101* RNAi females and males in control versus *DC352/+* genetic backgrounds. *DC532* is a transgenic duplication that covers *Atg101*. Note that the penetrance of the eye phenotype obtained from this experiment is lower than in those shown in **Fig. 3F** and **Table S1**. The reason for this difference stems from the fact that in the rescuing experiment *Dcr-2* was not overexpressed. (**B**) The presence of *DC352* largely rescues autophagic activity in *Atg101* RNAi eye disc samples. Bars represent mean ±S.D., *: $P<0.05$; two-sample Student t test or t test for unequal variances.

Genotypes: control=*w*; ey-Gal4(II)/+*. *Atg101* RNAi=*w*; ey-Gal4(II)/Atg101* RNAi *(KK101226)*. *Atg101* RNAi; DC352=*w*; ey-Gal4(II)/Atg101* RNAi *(KK101226); DC352/+*.

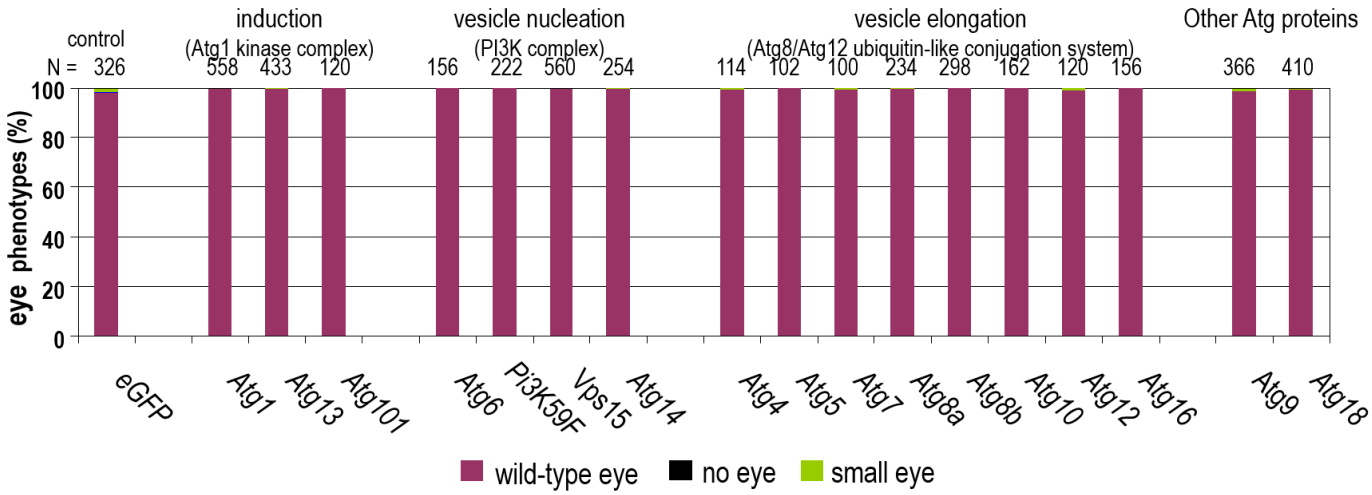

Figure S16. Silencing of *Atg* genes in the peripodial membrane only does not affect eye development. *Atg* genes and the number of samples examined are indicated. *RNAi* constructs were driven by *c311-Gal4* (see also in **Fig. S5E**). Knockdown of *eGFP* (control) leads to aberrant eye morphology at the largest extent (1.84%) among the samples. Data are also shown in **Table S2**.

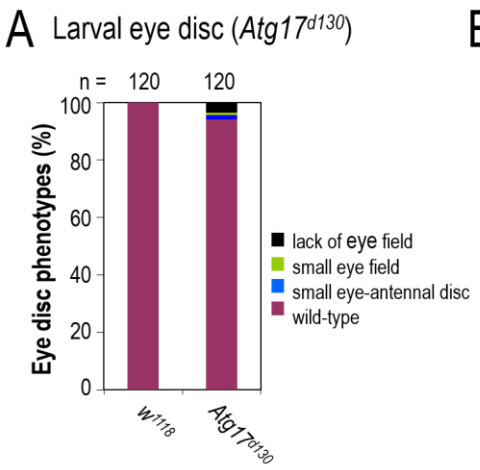

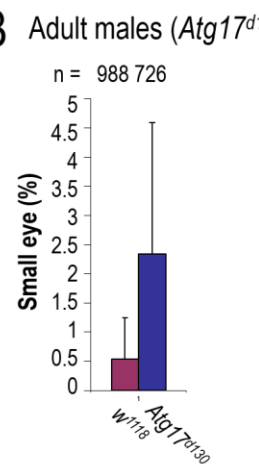

Genotype: *ey-Gal4, UAS-FLP/+; FRT82B GMR-hid, l(3)CL-R1/FRT82B, Atg17^{d130}*

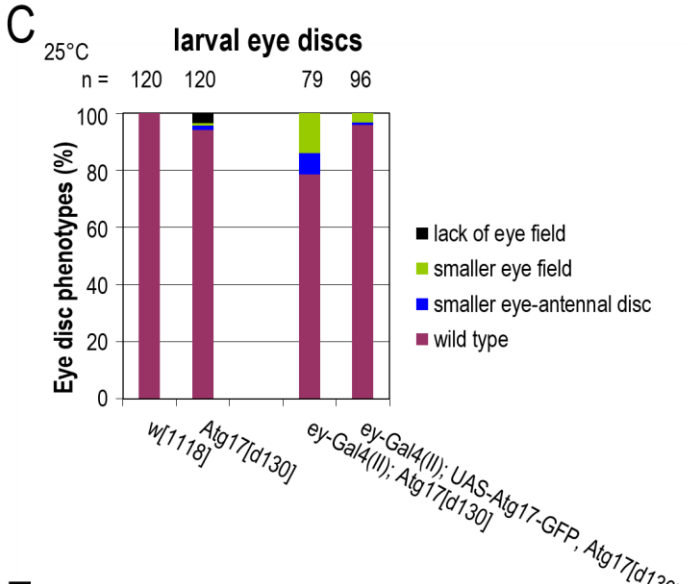

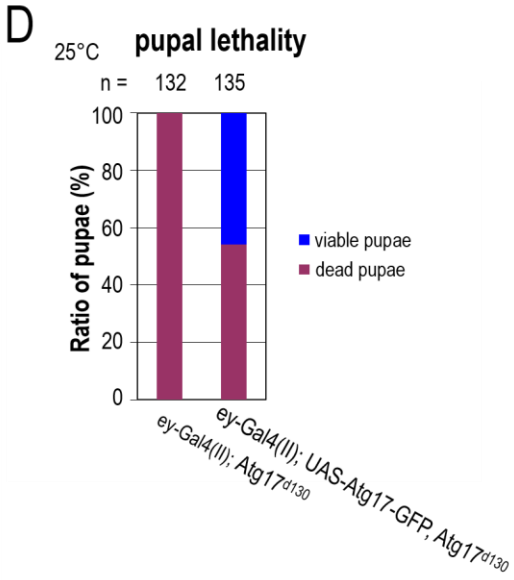

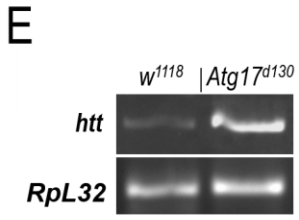

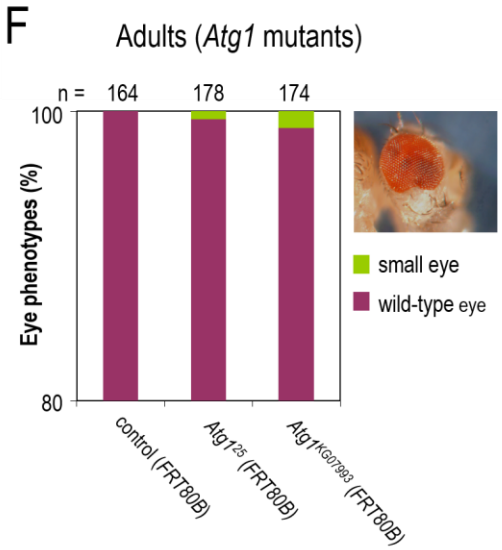

Genotype: *ey-FLP; RpS174 FRT80B/Atg1KG072993, FRT80B*

Figure S17. Mutational inactivation of *Atg1* and *Atg17* can interfere with eye development. (**A**) Loss-of-function (lf) mutation in *Atg17* compromises eye development with only a low penetrance. Eye disc samples were prepared from L3W larvae. (**B**) Penetrance of the small eye phenotype in *Atg17* mutant adult males. Bars represent mean ±S.D., ***: $P<0.005$; two-sample Student *t* test. (**C**) The eye disc morphology phenotype of $Atg17^{d130}$ mutant larvae can be rescued by a transgene containing the wild-type copy of *Atg17*. (**D**) The same transgene (*Atg17-GFP*) significantly suppresses the lethality of $Atg17^{d130}$ mutant pupae. Nearly half of the transgenic animals remains alive. (**E**) In $Atg17^{d130}$ mutant animals, the *htt* (*huntingtin*) gene becomes overexpressed, as compared with the control background. *htt* encodes a scaffold protein for selective autophagy. Atg17 also acts as a scaffold to recruit other Atg proteins to the phagophore assembly site. *RpL32* was used as an internal control (**F**) Penetrance of the small eye phenotype in *Atg1* lf mutant adult animals. The image shows a small eye. In panels **A** to **F**, the number of samples assayed is indicated. Genotypes: control in panel (B): *w*; ey-Gal4, UAS-FLP/+; FRT82B, GMR-hid, l(3)CL-*R^{1}*/ FRT82B*. $Atg17^{d130}$ = *w*;ey-Gal4, UAS-FLP/+; FRT82B, GMR-hid, l(3)CL-*R^{1}*/ FRT82B,* $Atg17^{d130}$. Control in panels (**C** and **D**): *ey-Gal4(II);* $Atg17^{d130}$ *= ey-Gal4 (II)/+*; *FRT82B,* $Atg17^{d130}$. *ey-Gal4(II);* $Atg17^{d130}$*, UAS-Atg17-GFP = ey-Gal4 (II)/+*; *FRT82B,* $Atg17^{d130}$*/*$Atg17^{d130}$*, UAS-Atg17-GFP*. Control in panel (**F**): *ey-FLP;* $RpS17^{4}$*, w+, FRT80B/FRT80B.* $Atg1^{25}$ *= ey-FLP;* $RpS17^{4}$*, w+, FRT80B/*$Atg1^{25}$*, FRT80B.* $Atg1^{KG07993}$ *= ey-FLP;* $RpS17^{4}$*, w+, FRT80B/*$Atg1^{KG07993}$*, FRT80B.*

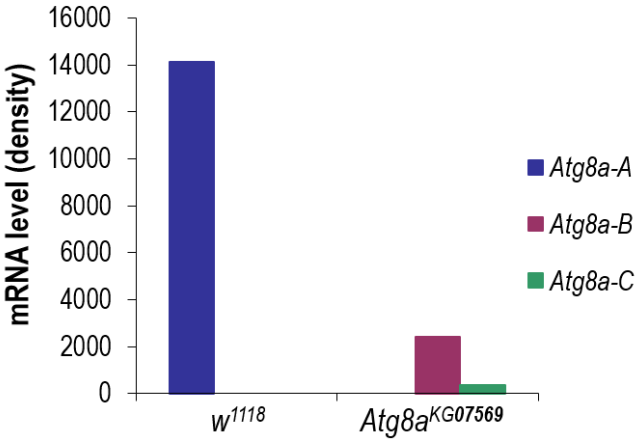

Figure S18. Relative amounts of the different *Atg8a* mRNA isoforms in wild-type (w^{1118}) versus an *Atg8a-A* mutant background. Quantification of band intensities shown in **Fig. 4A'** and **B**. In the control sample, only *Atg8a-A* (blue bar) is active. In the *Atg8a-A* mutant background, *Atg8a-A* transcript disappears, *Atg8a-B* mRNA (purple bar) becomes abundant, while *Atg8a-C* (green bar) is slightly activated. *Act5C* was used as an internal control.

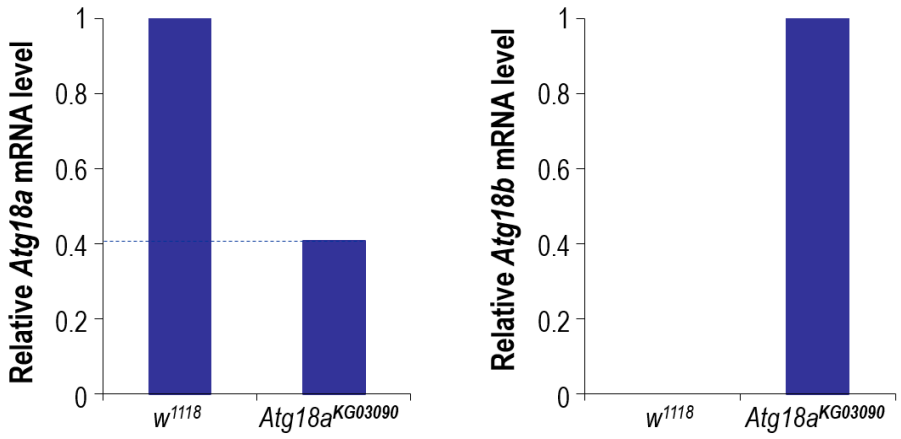

Figure S19. Relative amounts of *Atg18a* and *Atg18b* transcripts in wild-type (w^{1118}) versus an *Atg18a*-specific mutant background. Quantification of band intensities shown in **Fig. 4E**. Left panel: *Atg18a* mRNA levels are highly reduced in mutant samples, as compared with control (w^{1118}). Right panel: *Atg18b* mRNA is not detectable in control samples, but is readily visible in mutant samples. $Atg18a^{KG03090}$ = $Atg18a^{KG03090}$/*Atg18a Df(3L)Exel6112*. *Act5C* was used as an internal control.

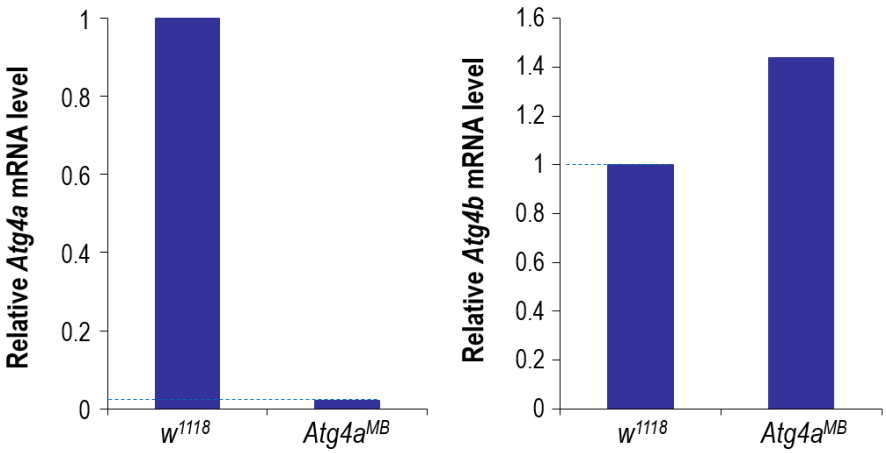

Figure S20. Relative amounts of *Atg4a* and *Atg4b* mRNAs in control versus an *Atg4a* lf mutant background. Quantification of band intensities shown in **Fig. 4F**. Left panel: *Atg4a* mRNA levels are highly reduced in mutant samples, as compared with controls. Right panel: *Atg4b* is expressed at higher levels in *Atg4a* mutant samples than in control ones. *Act5C* was used as an internal control. Control: w^{1118}. $Atg4a^{MB}$: $Atg4a^{MB03551}$.

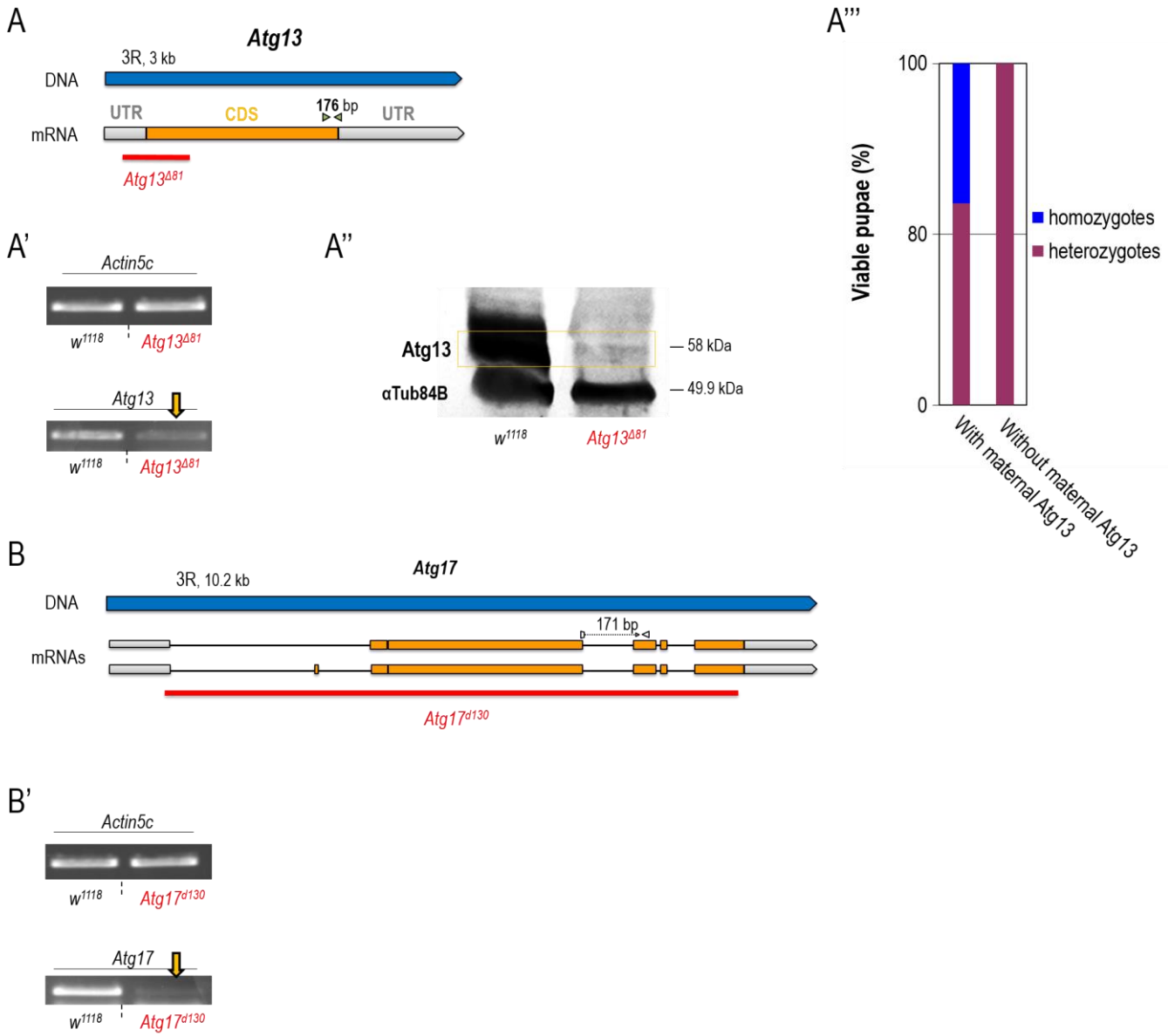

Figure S21. Presence of *Atg13*- and *Atg17*-specific transcripts and proteins in *Atg13* and *Atg17* mutant eye disc samples, respectively. (**A**) The structure of *Atg13* gene. (**A'**) Presence of *Atg13* transcripts in $Atg13^{\Delta 81}$ mutant samples (yellow arrow). (**A''**) Anti-Atg13 antibody staining reveals the presence of Atg13 proteins in $Atg13^{\Delta 81}$ mutant samples. (**A'''**) Without maternally contributed *Atg13*, homozygous mutants die prior to the L3W stage. ovo^{D1}

mutation eliminates the maternal *Atg13* products (dominant female sterile technique). Left column shows the progeny of the following cross: *hsFLP; FRT82B, Atg13$^{\Delta 81}$/TM6B* x *FRT82B, Atg13$^{\Delta 81}$/TM6B.* Right column displays progeny of the following cross: *hsFLP; FRT82B, Atg13$^{\Delta 81}$/FRT82B, ovo^{D1}* x *FRT82B, Atg13$^{\Delta 81}$/TM6B* heat shock (2 h, 2 times at 37°C during larval stages). (**B**) The structure of *Atg17* gene. In panels **A** and **B**, both coding region (DNA) and transcript (mRNA) are shown. Yellow boxes indicate coding exonic sequences, connecting lines correspond to introns, grey boxes refer to UTRs. Red lines show the extend of deletions examined, primers used for semi-quantitative RT-PCR are also indicated. (**B'**) The presence of *Atg17* transcripts (yellow arrow) in *Atg17* null mutant samples. In panels **A'** and **B'**, *Act5C* was used as an internal control. In panel **A''**, αTub84B was used as an internal control.

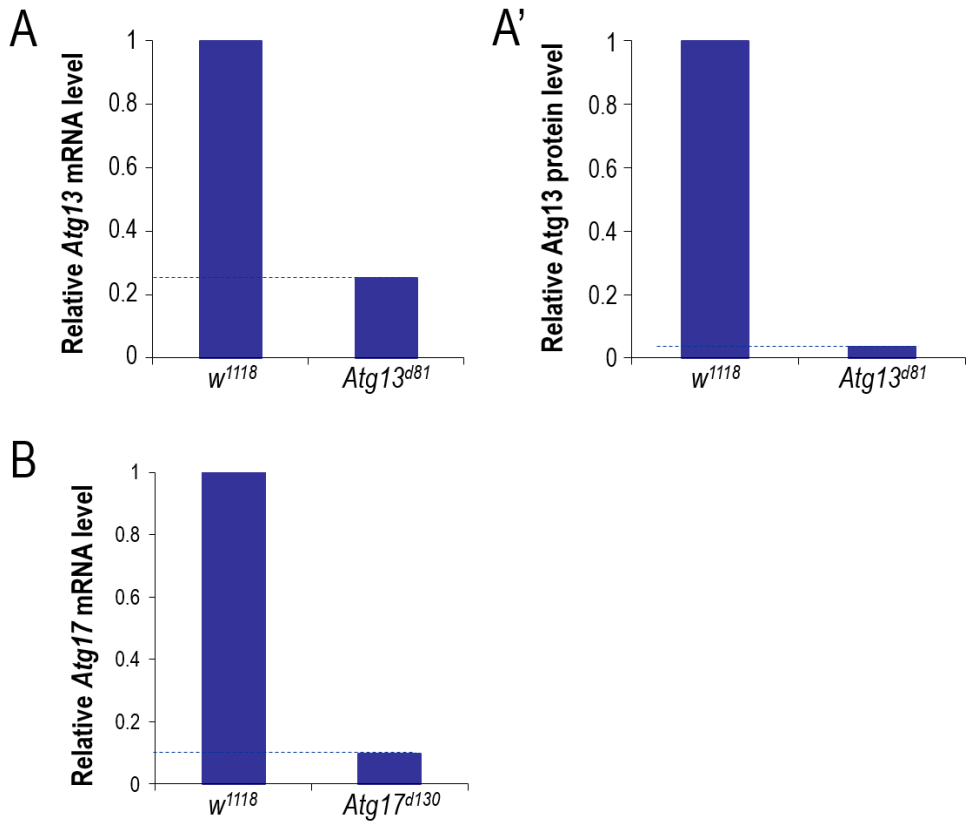

Figure S22. Relative amounts of *Atg13*- and *Atg17*-specific gene products in *Atg13* and *Atg17* mutant eye disc samples, respectively. Quantification of band intensities shown in **Fig. S21A'**, **A''**, **B'**. (**A**) *Atg13* transcript levels are lowered in *Atg13* lf mutant samples, as compared with controls. (**A'**) Low, but still detectable, amount of Atg13 proteins in *Atg13* lf mutant samples. (**B**) Relative *Atg17*-specific mRNA levels in control versus *Atg17* null mutant samples. *Act5C* was used as an internal control.

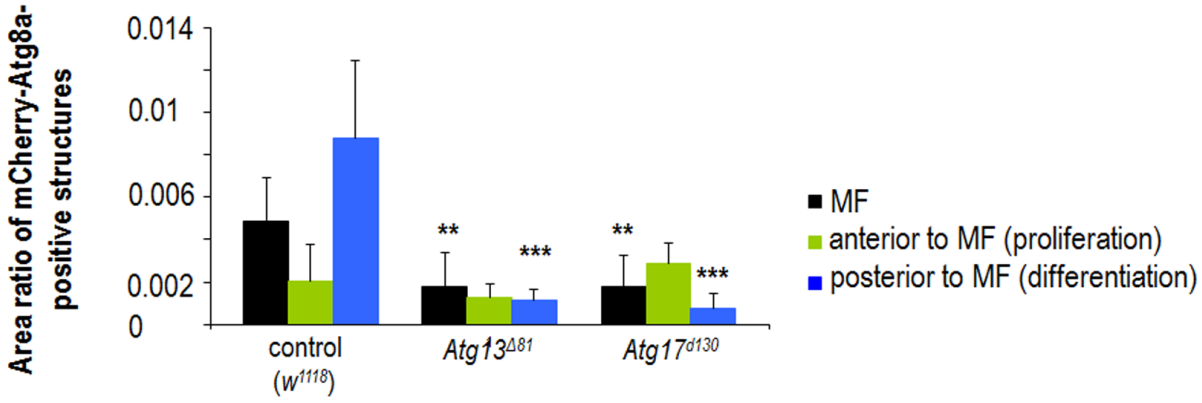

Figure S23. Relative amount of mCherry-Atg8a-positive autophagic structures in *Atg13* and *Atg17* mutant eye disc samples. The amount of autophagic structures decreased significantly, but was not eliminated completely, in the mutant samples. Bars represent mean ±S.D., **: $P<0.01$, **: $P<0.001$, two-sample Student t test or t test for unequal variances. The mutant alleles represent large deletions, thereby considered as genetic null mutations.

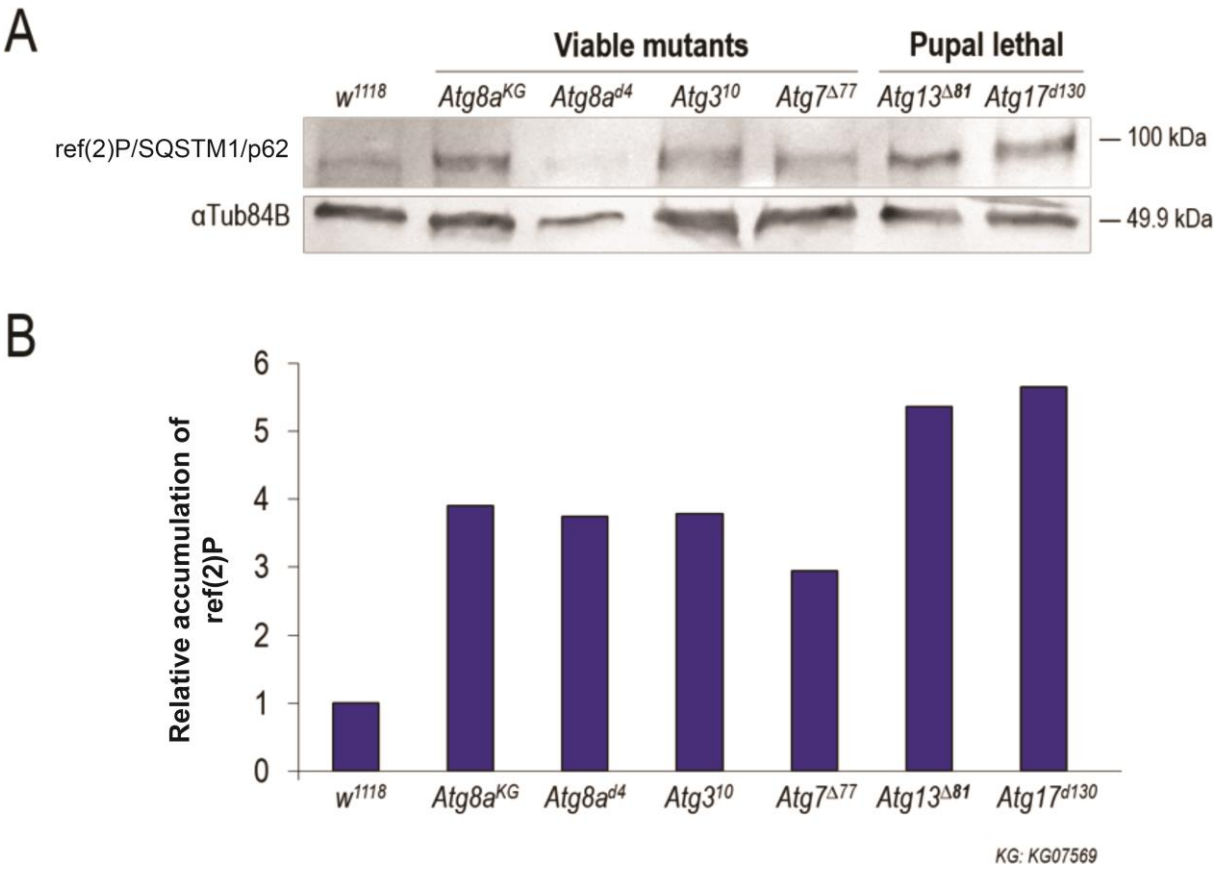

Figure S24. ref(2)P (also termed SQSTM1/p62 in mammals) protein levels vary among different *Atg* mutant eye disc samples. (**A**) Western blot analysis showing relative amounts of ref(2)P/SQSTM1/p62 proteins in *Atg* mutant samples. ref(2)P/SQSTM1/p62 served as a substrate for autophagy (*i.e.* its amount is inversely proportional with autophagic activity). αTub84B was used as an internal control. Control: w^{1118}. Pupal lethal homozygous mutants are derived from heterozygous parents. (**B**) Quantification of band intensities shown in panel **A**. The amount of ref(2)P/SQSTM1/p62 is highest in mutants exhibiting most severe phenotypic effects, $Atg13^{\Delta 81}$ and $Atg17^{d130}$ (pupal lethal). Thus, the other *Atg* mutants (viable) examined cannot be considered as complete autophagy-defective samples (they display residual activities).

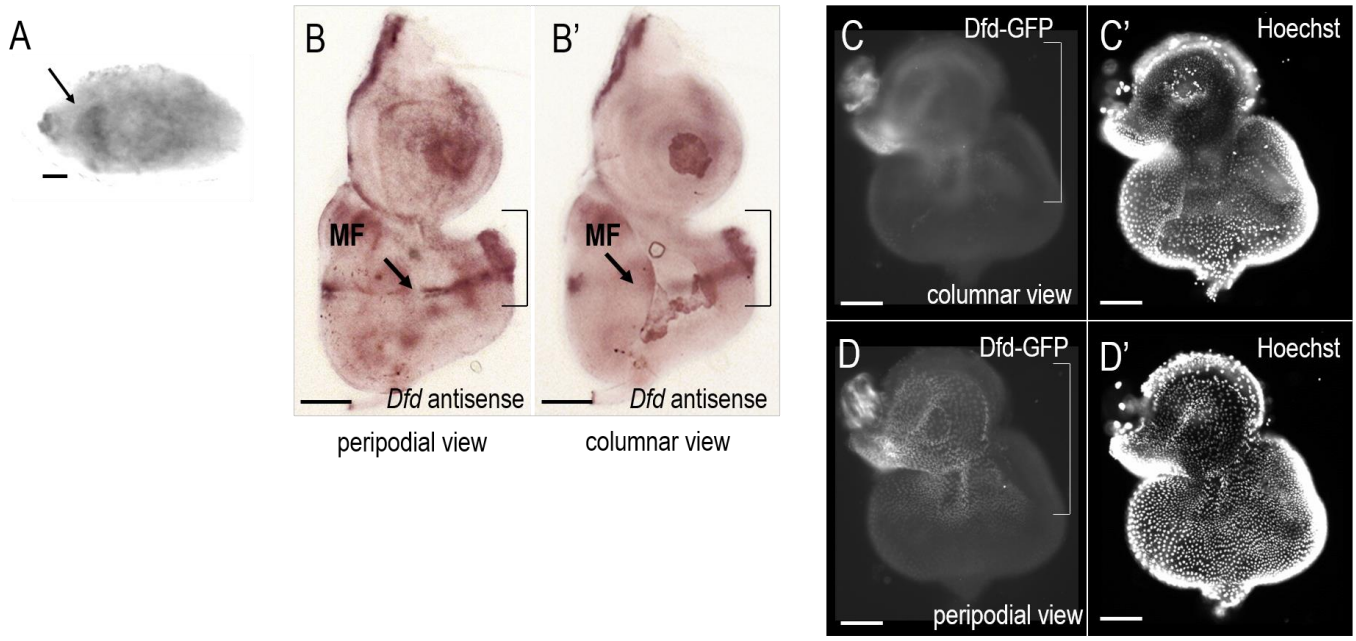

Figure S25. *Dfd* is expressed in the peripodial membrane. (**A)** *Dfd* expression in a 9-h embryo. The arrow points to the *Dfd*-positive area. (**B**, **B'**) Expression of *Dfd* in the eye disc. Brackets indicate the area where *Dfd* mRNA is detectable. (**C**, **D)** Dfd-GFP protein accumulates only in the peripodial membrane (sharp signs can only be seen in the nuclei of panel **D**). (**C'**, **D'**) Hoechst staining indicates nuclei, antenna part is up. Bars: 50 µm in each image. Genotype (**A**, **B**, **B'**): w^{1118}; (**C** to **D'**): *Dfd-GFP*.

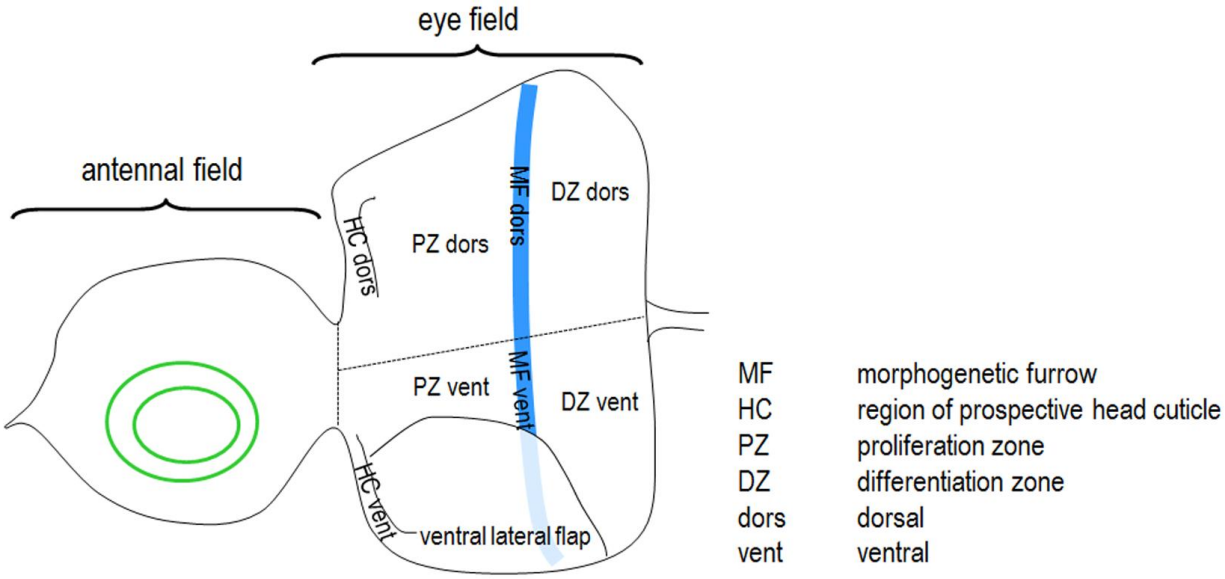

Figure S26. The eye field is divided into 9 parts (subfields) for analyzing the expression of *Atg8a-A* reporters (see on Fig. 6G’’’). The following subregions were analyzed: 1, dorsal differentiation zone (DZ dors); 2, ventral differentiation zone (DZ vent); 3, dorsal morphogenetic furrow (MF dors.); 4, ventral morphogenetic furrow (MF vent); 5, dorsal proliferation zone (PZ dors); 6, ventral proliferation zone (PZ vent); 7, dorsal prospective head cuticle (HC dors); 8, ventral prospective head cuticle (HC vent); 9, ventral lateral flap.

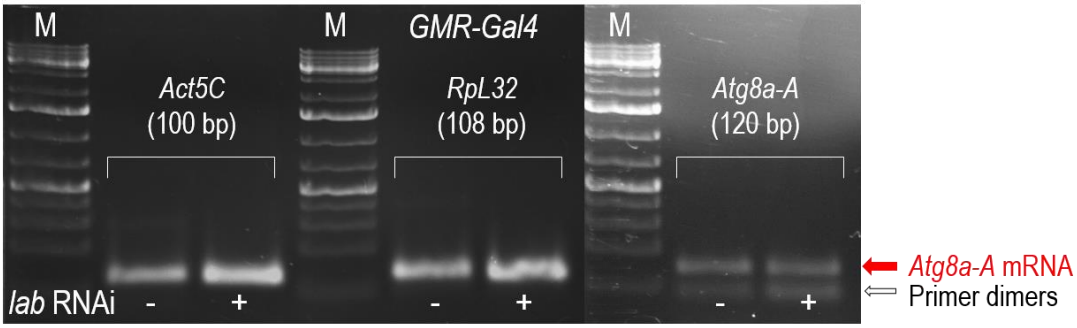

Figure S27. The lab (labial) protein does not influence *Atg8a-A* transcription in the differentiation zone. Semi-quantitative RT-PCR on control versus *lab* RNAi eye disc samples displays no significant difference between transcript levels. The construct is driven by *GMR-Gal4* that is active only in the DZ (also see **Fig. S4A**). *Act5C* and *RpL32* were used as internal controls. M, molecule size marker. Eye-antennal disc samples were dissected from L3W larvae. Control: *w*; GMR-Gal4/+*, *UAS-Dcr-2/+*. *lab* RNAi: *w*; GMR-Gal4/lab* RNAi, *UAS-Dcr-2/+*.

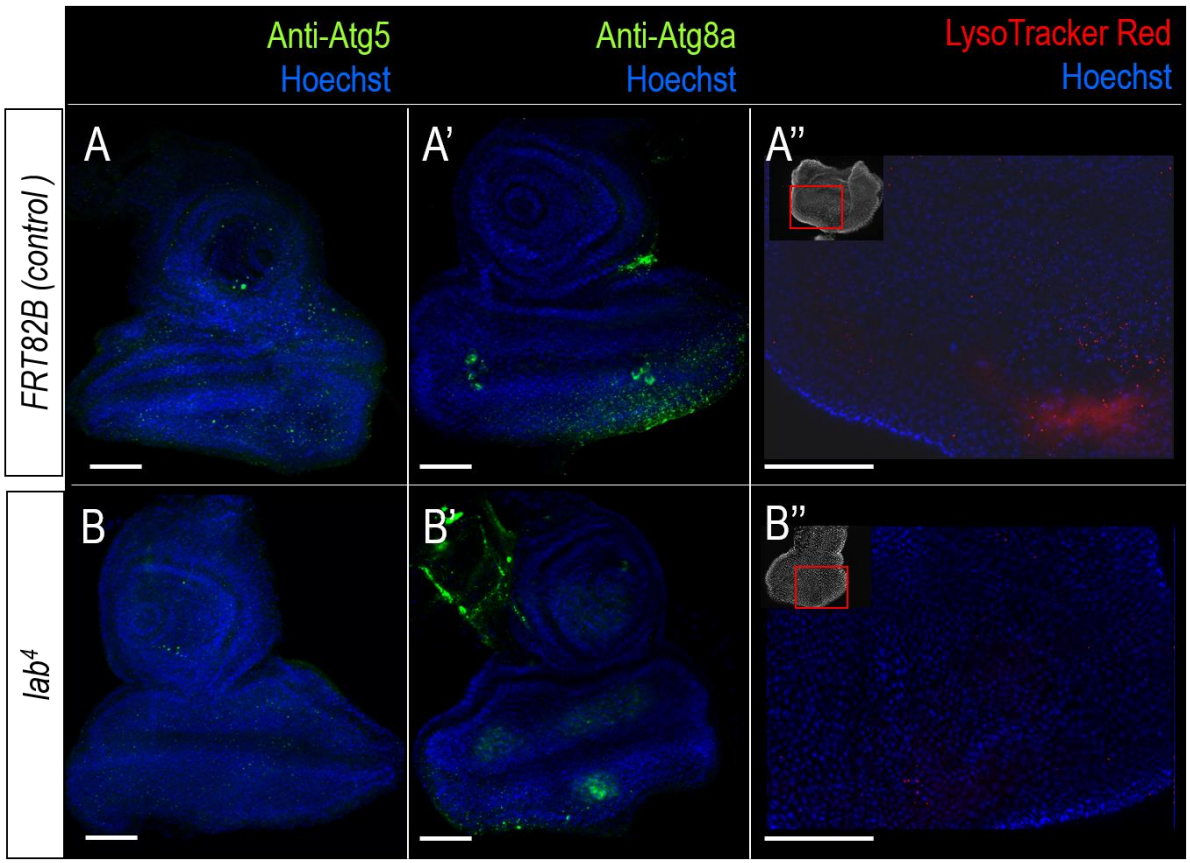

Figure S28. Mutational inactivation of *lab* leads to reduced autophagic activity in the differentiation zone. (**A**) Anti-Atg5 antibody labels early autophagic structures in the eye disc of a *FRT82B* control animal. (**A'**) Anti-Atg8a staining reveals autophagosomes and autolysosomes in the eye disc of a *FRT82B* animal. (**A''**) LysoTracker Red-positive autophagic structures accumulate mainly in the differentiation zone (DZ). (**B** to **B''**) In *lab*^{4} mutant samples, the number of autophagic structures decreases significantly in the DZ, as compared with control samples. Quantification of data is shown in **Fig. 8F**. At the upper left corner in panels **A'''** and **B'''**, the entire eye-antenna imaginal disc is visible, and a red rectangle shows the enlarged area. Eye disc samples were dissected from L3W larvae; bars: 50 µm. FRT82B = *w*, ey-FLP*; *FRT82B, l(3)cl-R3*^{1}*/FRT82B*. *lab*^{4} = *ey-FLP; FRT82B, l(3)cl-R3*^{1}*/FRT82B, lab*^{4}.

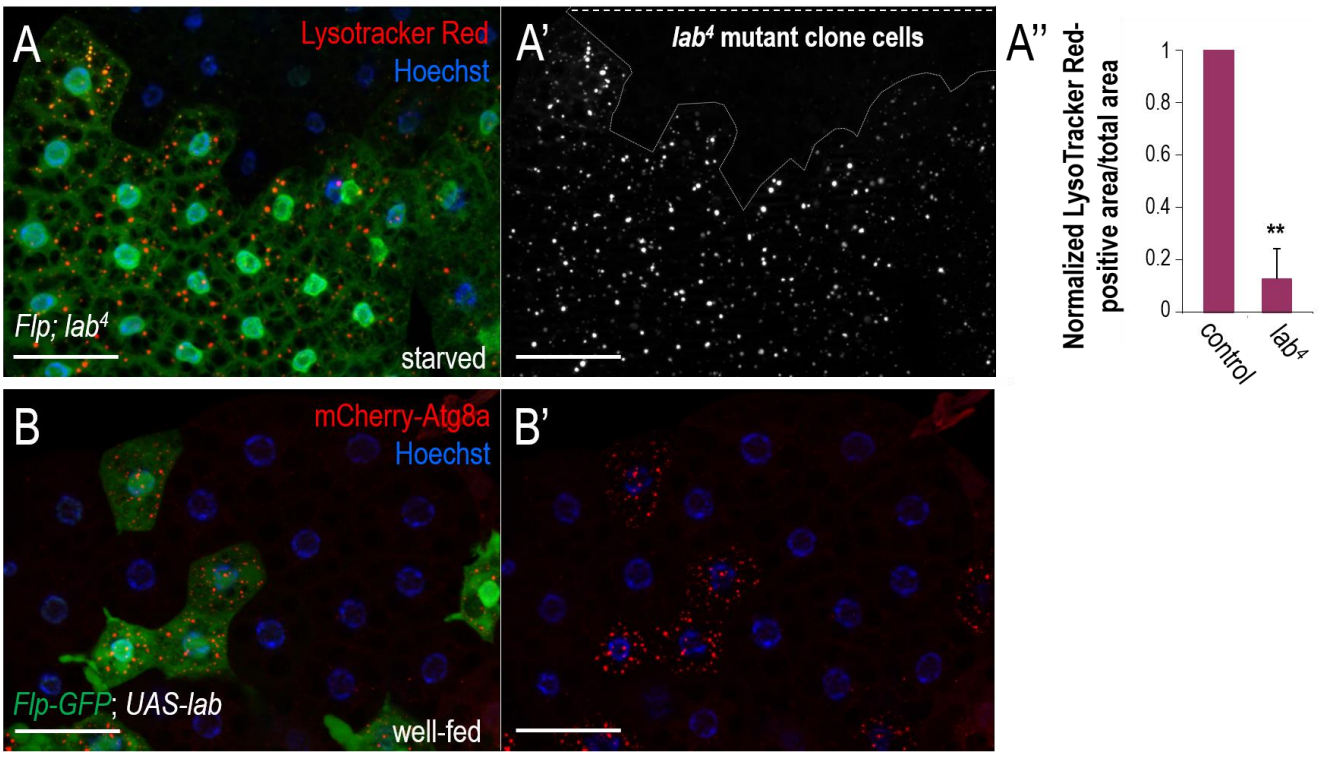

Figure S29. lab activates autophagy in the larval fat body. (**A**) Clonal inhibition of *lab* (non-green cells) causes elimination of autophagic (LysoTracker Red-positive) structures in the affected cells under conditions of starvation. Non-green cells are defective for *lab*. Green cells serve as controls. (**A'**) The corresponding uncolored figure. (**A''**) Quantification of autophagic structures in control versus lab^4 mutant fat body cells. Bars represent mean ±S.D., **: $P<0.01$, paired t test. (**B**, **B'**) Clonal hyperactivation of *lab* in the larval fat body induces the amount of mCherry-Atg8a-positve autophagic structures (red foci) in the affected cells under well-fed conditions. Hoechst staining indicates nuclei, bars: 50 µm. Fat body samples were prepared from 88 to 92-h L3F-stage larvae. Temperatures were 25°C. Genotypes: in panel (**A**): non-green cells: *w*, hsFLP; FRT82B, lab*^{4}. green, control cells: *w*, hsFLP; FRT82B, Ubi-GFP* or *w*, hsFLP; FRT82B, Ubi-GFP / FRT82B, lab*^{4}. In panel (B) green cells: *w*, hsFlp; UAS-lab/+; ActGal4, UAS-nlsGFP, r4-mCherry-Atg8a*. Non-green, control cells: *w*, hsFlp; UAS-lab/+; Act<CD2<Gal4, UAS-nlsGFP, r4-mCherry-Atg8a*.

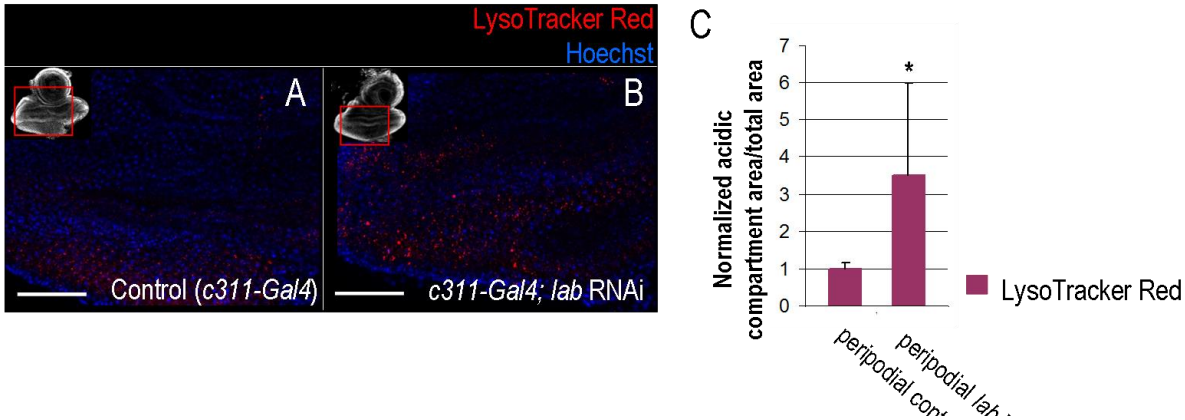

Figure S30. Depletion of *lab* in the peripodial membrane increases the amount of acidic compartments in the eye disc. (**A**) LysoTracker Red staining of a *c311-Gal4/UAS-Dcr-2* eye disc, serving as a control for *lab* RNAi. Red foci indicate lysosomes, autolysosomes and multivesicular bodies (acidic compartments). (**B**) LysoTracker Red staining of *lab* RNAi/+; *c311-Gal4/UAS-Dcr-2* eye disc shows an elevated amount of acidic compartments. In panels **A** and **B**, the antenna part is up. At the upper left corner, the entire eye-antenna imaginal disc is shown, and red rectangle indicates the enlarged area. Eye disc samples were dissected from L3W larvae; bars: 50 µm. (**C**) Quantification of autophagic structures in eye disc samples depleted for *lab* only in the peripodial membrane. The ratio of LysoTracker Red-positive structures and the entire eye disc is on average, data were normalized to controls. Bars represent mean ±S.D., *: $P<0.05$, t test for unequal variances.

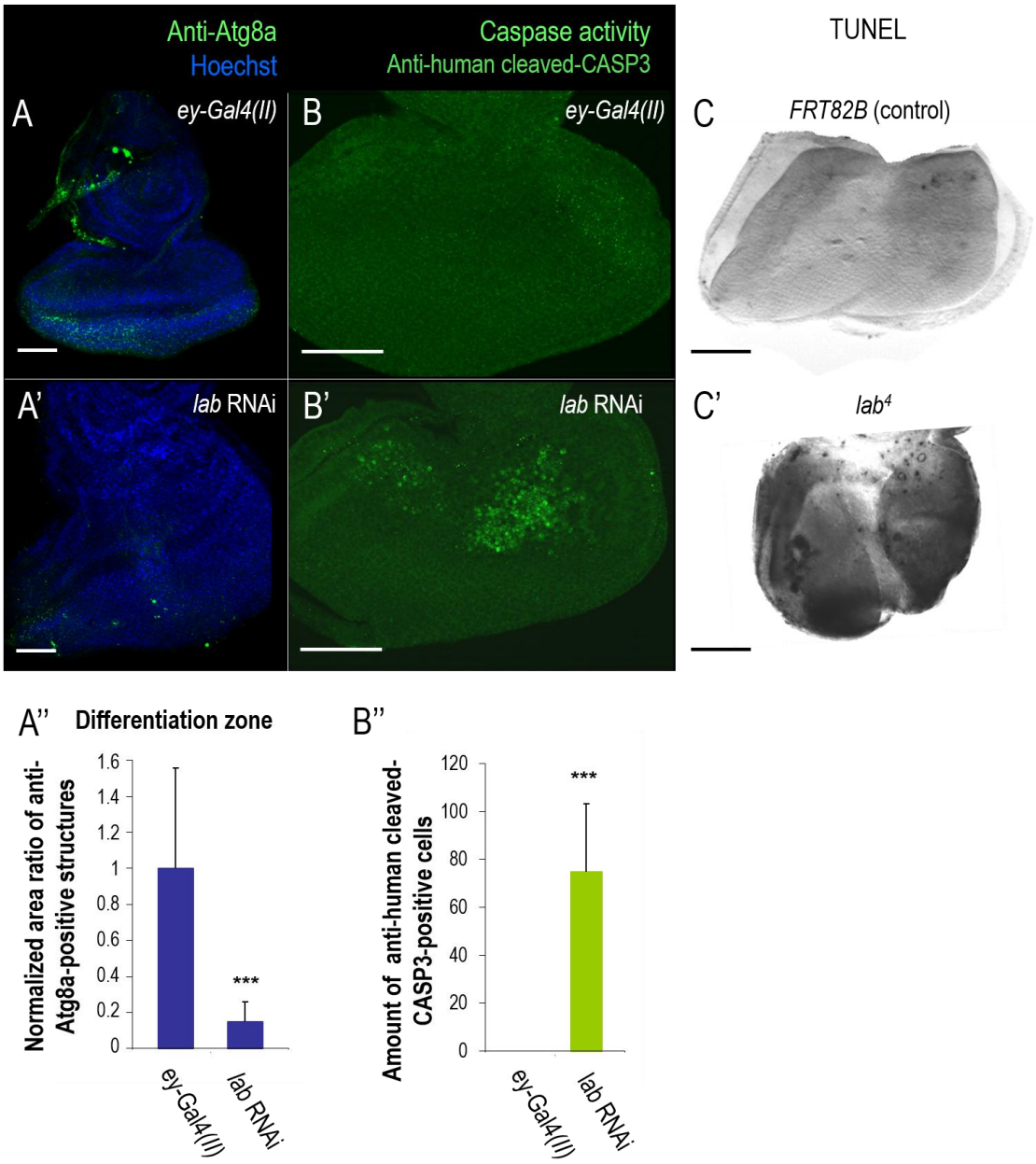

Figure S31. Lab deficiency in the eye disc decreases the amount of Atg8a-positive autophagic structures, and increases the number of cells with apoptotic features. (**A**, **A'**) Anti-Atg8a staining indicates autophagic structures (green foci) in control versus *lab* RNAi samples. *lab* RNAi construct is driven by *ey-Gal4(II), UAS-Dcr-2(II)* (**A''**) Quantification of autophagic structures in control [*ey-Gal4(II)*] versus *ey-Gal4(II); lab* RNAi samples. (**B**, **B'**) Human cleaved-CASP3 antibody staining in control and *lab* RNAi samples. Green foci

indicate cells, which show increased caspase activity hence probably undergo apoptosis. (**B''**) Quantification of cells which show increased caspase activity in samples indicated. (**C**, **C'**) TUNEL staining in control versus *lab* mutant samples. In panels **A''** and **B''**, bars represent mean ±S.D., ***: $P<0.005$; Mann-Whitney U-test. FRT82B = *w*, ey-FLP*; *FRT82B, l(3)cl-R3^{1}/FRT82B. lab^{4} = ey-FLP; FRT82B, l(3)cl-R3^{1}/FRT82B, lab^{4}*.